10

Theory of Polychromatic Reconstruction for Volume Holographic Memory

Ryushi Fujimura, Tsutomu Shimura and Kazuo Kuroda
Institute of Industrial Science, The University of Tokyo
Japan

1. Introduction

In volume holographic memory (van Heerden, 1963), the information is stored as a volume hologram and retrieved through the holographic reconstruction process by illuminating the hologram with a readout probe beam whose wavelength, incident angle, and wavefront should be identical to those of the reference beam used in the recording process. This requirement stems from the fact that diffraction from the volume hologram is restricted by Bragg's law. While such a restriction is responsible for the large storage density of volume holographic memories, it also causes some obstacles for implementing practical memory systems. For example, in rewritable recording media, like photorefractive materials, illumination with a readout probe beam will rewrite the recorded hologram, destroying the stored information. Even in a photopolymer, some of the storage capacity will be wasted during the readout if some monomers still exist in the readout volume. These issues are obviously caused by the destructive probe beam having the ability to expose the recording medium in a similar manner to the recording beam.

To avoid such a problem, several nondestructive readout methods have been proposed so far (Gulanyan et al., 1979; Petrov et al., 1979; Külich, 1987), where the readout is performed at a longer wavelength, outside the sensitive spectral region of the recording material. These methods can successfully reconstruct the stored image at a wavelength different from the recording one, but most of these methods may not be practical for holographic memory systems because the multiplexing capability is considerably lowered. For example, anisotropic diffraction (Petrov et al., 1979) requires a specific recording configuration and thus limits the number of multiplexed pages. A spherical probe beam method (Külich, 1987) tends to produce severe crosstalk noise from other multiplexed pages, which demands a large angular separation between two adjacent multiplexed holograms, resulting in a small storage density.

Recently, we proposed another way to reconstruct an image at a different wavelength (Fujimura et al., 2007). Our method, which we call polychromatic reconstruction (PCR), utilizes a spectrally broad light source for the probe beam, as shown in Fig. 1. Each angular spectral component of the recorded gratings can be Bragg-matched with one particular wavelength within the broadband spectrum of the probe beam. Thus, the whole image can be reconstructed from the volume hologram even though the probe wavelength is very different from the recording one. On the other hand, analogous to the spherical probe beam

method, the large spectral width of the polychromatic probe beam causes deterioration of the angular selectivity and results in considerable lowering of the multiplexing capability. However, unlike the case of the spherical probe beam, such a drawback can be overcome by using a selective detection method (Fujimura et al., 2010). If the proper optical component, such as a wavelength filter or grating, is additionally inserted in the imaging system, we can detect the signal image alone even though the crosstalk-noise waves are diffracted from other multiplexed pages. Therefore, PCR with the selective detection method is a promising way to achieve nondestructive readout in volume holographic memories without sacrificing the multiplexing capability.

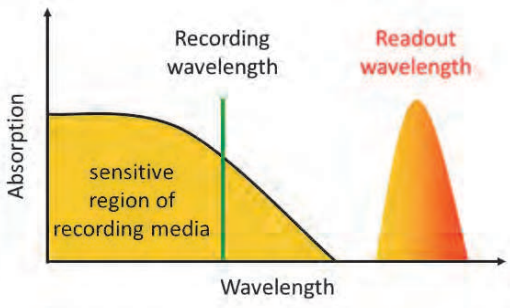

Fig. 1. Concept of the nondestructive readout in the PCR method.

When we implement the PCR method in a holographic memory system, it is important to know the properties of the holographic reconstruction process with the polychromatic light. Indeed, the PCR method shows several notable features as compared with conventional monochromatic reconstruction. For example, the reconstructed image has a wavelength distribution that linearly shifts along the grating vector, and image magnification occurs in a direction perpendicular to the incident plane. In fact, knowledge of the required bandwidth of the polychromatic probe beam is essential to design a practical memory system.
In this chapter, we develop the theory of holographic reconstruction with polychromatic light, especially from the viewpoint of its application to volume holographic memory. Based on the plane-wave expansion model, we will derive expressions for the required bandwidth, the distortion of the reconstructed image, the optimum recording configuration, the diffraction efficiency, the inter- and intra-page crosstalk noise, and the theoretical limit of the storage density. The obtained expressions show unique features of the PCR method and are very informative for constructing actual holographic memory systems utilizing the PCR method.

2. Basic principle of the image reconstruction

2.1 Reconstruction from a plane-wave hologram

First we consider the diffraction from a plane-wave hologram that is formed by signal and reference plane waves. When the grating recorded at a wavelength λ_w is read out with a probe wavelength λ_p, the Bragg condition is given by

$$k_p\left(\mathbf{e}_d-\mathbf{e}_p\right)=k_w\left(\mathbf{e}_s-\mathbf{e}_r\right)\equiv k_w\mathbf{G}, \tag{1}$$

where $\mathbf{e}_s$, $\mathbf{e}_r$, $\mathbf{e}_p$, and $\mathbf{e}_d$ are the unit direction vectors of the signal, reference, probe, and diffracted plane waves, respectively; $k_q = 2\pi n_q/\lambda_q$ ($q = w, p$) is the wave number at the wavelength λ_q and the refractive index n_q; and $\mathbf{G}$ is the grating vector normalized by the recording wave number k_w. In order to obtain diffraction from the grating $\mathbf{G}$, the unit direction vector $\mathbf{e}_p$ and the probe wavelength λ_p should be properly chosen so as to satisfy Eq. (1). Such a restriction can be derived from Eq. (1) and the relation $|\mathbf{e}_d|^2 = 1$, which is written as

$$\left(\mathbf{e}_p + \frac{\mu}{2}\mathbf{G}\right)\cdot\mathbf{G} = 0, \tag{2}$$

where μ is the ratio of the wave numbers of the recording and probe beams, i.e., $\mu = k_w/k_p$. Hereafter, for simplicity, we assume that wavelength dispersion of the refractive index can be neglected, i.e., $n_w \approx n_p \approx n$, and thus, μ can be approximated by the ratio of wavelengths. If $\mathbf{e}_p$ and λ_p satisfy Eq. (2), the grating will reproduce the plane wave with the unit direction vector $\mathbf{e}_d$ expressed as

$$\mathbf{e}_d = \mathbf{e}_p + \mu\mathbf{G}. \tag{3}$$

Generally, there are many combinations of $\mathbf{e}_p$ and λ_p that satisfy Eq. (2). Thus, it is possible to obtain diffraction from a plane wave hologram even when the readout probe wave vector is not identical to the reference wave vector in the recording process, i.e., $\lambda_p \neq \lambda_w$ or $\mathbf{e}_p \neq \mathbf{e}_r$. For example, when the probe wavelength λ_p is given, the incident angle of the probe beam should be adjusted so that the vector $\mathbf{e}_p + \mu\mathbf{G}/2$ lies on the plane normal to the grating $\mathbf{G}$, as shown in Fig. 2. Note that there is a maximum value for the allowed λ_p because the relation $\mu|\mathbf{G}|/2 < 1$ should hold, as is seen from Fig. 2. In this case, the trace of $\mathbf{e}_p$ forms a circle, which is regarded as the Bragg degeneracy.

On the contrary, when $\mathbf{e}_p$ is given, the probe wavelength λ_p should satisfy the following relation:

$$\mu = -\frac{2\mathbf{e}_p\cdot\mathbf{G}}{|\mathbf{G}|^2}. \tag{4}$$

Note that, in this case, the wavelength ratio μ is uniquely determined by the set of ($\mathbf{e}_p$, $\mathbf{G}$).

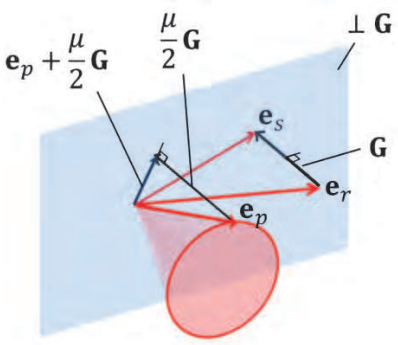

Fig. 2. The possible choice of the incident angle of the probe beam to reconstruct the plane wave hologram represented by $\mathbf{G}$.

2.2 Reconstruction of the image information

A volume holographic memory usually stores two-dimensional image information. Therefore, the signal beam consists of many plane waves and creates various grating vectors after interfering with the reference plane wave. We express the i-th signal component $\mathbf{e}_{si}$ as $\mathbf{e}_{si} = \mathbf{e}_{s0} + \boldsymbol{\delta}\mathbf{e}_{si}$, where $\mathbf{e}_{s0}$ is the central direction vector of the diverged signal beam, and $\boldsymbol{\delta}\mathbf{e}_{si}$ is the deviation vector from $\mathbf{e}_{s0}$. Similarly, the corresponding diffracted component $\mathbf{e}_{di}$ is expressed as $\mathbf{e}_{di} = \mathbf{e}_{d0} + \boldsymbol{\delta}\mathbf{e}_{di}$. In this case, the Bragg condition for each angular spectral component is given by

$$k_p\left(\mathbf{e}_{di} - \mathbf{e}_p\right) = k_w\left(\mathbf{e}_{si} - \mathbf{e}_r\right) \equiv k_w \mathbf{G}_i \,, \tag{5}$$

where $\mathbf{G}_i$ is the normalized grating vector for i-th component. In order to reproduce the whole image, the Bragg condition of Eq. (5) should be satisfied at all components i. If we assume that Eq. (5) is satisfied at the central signal component ($i = 0$) and that the divergence angle of the signal beam is sufficiently small, i.e., the relation $|\boldsymbol{\delta}\mathbf{e}_{si}|^2 << 1$ holds, then Eq. (2) can be rewritten as

$$\left(\mathbf{e}_p + \frac{\mu}{2}\mathbf{G}_i\right)\cdot\mathbf{G}_i \approx \mathbf{e}_{d0}\cdot\boldsymbol{\delta}\mathbf{e}_{si} \,. \tag{6}$$

In order to satisfy the Bragg condition at any component i, the probe wave vector should be identical to the reference wave vector (i.e., $\lambda_p = \lambda_w$ and $\mathbf{e}_p = \mathbf{e}_r$) so that the relation $\mathbf{e}_{d0} = \mathbf{e}_{s0}$ holds. Otherwise, the obtained diffracted waves are limited to those from the components satisfying the relation $\mathbf{e}_{d0}\cdot\boldsymbol{\delta}\mathbf{e}_{sj} = 0$. Therefore, it is usually considered that the image information cannot be completely reproduced when the probe wavelength is different from the recording one.

However, there are two possible ways to satisfy Eq. (5) for all components even when $\lambda_p \neq \lambda_w$. One is Külich's approach (Külich, 1987), where a probe beam having adequate angular divergence is used instead of the plane wave. In this method, for each signal component i, there is a probe plane wave component $\mathbf{e}_{pi} = \mathbf{e}_{p0} + \boldsymbol{\delta}\mathbf{e}_{pi}$ that satisfies

$$\left(\mathbf{e}_{pi} + \frac{\mu}{2}\mathbf{G}_i\right)\cdot\mathbf{G}_i \approx \mathbf{e}_{d0}\cdot\left(\boldsymbol{\delta}\mathbf{e}_{si} + \frac{1}{\mu}\boldsymbol{\delta}\mathbf{e}_{pi}\right) = 0 \,, \tag{7}$$

where we assume that the divergence angles of the probe and signal beams are sufficiently small, and thus, the relations $|\boldsymbol{\delta}\mathbf{e}_{si}|^2 << 1$, $|\boldsymbol{\delta}\mathbf{e}_{pi}|^2 << 1$, and $\boldsymbol{\delta}\mathbf{e}_{pi}\cdot\boldsymbol{\delta}\mathbf{e}_{si} << 1$ hold. Then, the diffracted wave is reproduced as described by the following relation:

$$\mathbf{e}_{di} = \mathbf{e}_{pi} + \mu\mathbf{G}_i = \mathbf{e}_{d0} + \boldsymbol{\delta}\mathbf{e}_{pi} + \mu\boldsymbol{\delta}\mathbf{e}_{si} \,. \tag{8}$$

Note that, in this method, special care should be taken about the diffraction due to the Bragg degeneracy. If several probe components simultaneously satisfy Eq. (7) for one particular signal component, its grating component will produce several diffracted waves with different direction vectors, as represented by Eq. (8). This will degrade the quality of the reconstructed image. To avoid such a situation, the angular spectral components of the probe beam should exist on only one particular plane. For example, it is preferable that the probe beam should be expanded by using a cylindrical lens, not a spherical lens.

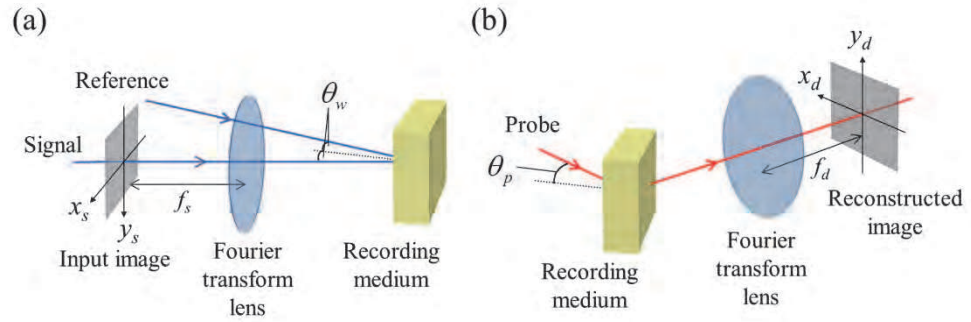

Fig. 3. Schematic diagram of (a) the recording and (b) the reconstruction schemes in the PCR method. θ_w is the internal half crossing angle of $\mathbf{e}_{s0}$ and $\mathbf{e}_r$; θ_p is the internal incident angle of $\mathbf{e}_p$; and f_s and f_d are the focal lengths of the Fourier transform lenses in the recording and reconstruction processes, respectively.

Another way to satisfy Eq. (5) is our approach, the PCR method. This method utilizes a broadband probe beam instead of monochromatic light. The recording and readout schemes of the PCR method are illustrated in Fig. 3. In the recording process, a monochromatic signal beam bearing the image information passes through a Fourier transform lens and records a Fourier hologram in the usual way. In the readout process, the recorded hologram is readout by using a spectrally broad but spatially coherent light source, such as a super luminescent diode (SLD). All grating components satisfy the Bragg condition because the probe beam includes a spectral component that satisfies the following relation for each component i:

$$\mu_i \equiv \frac{k_w}{k_{pi}} \approx \frac{\lambda_{pi}}{\lambda_w} = -\frac{2\mathbf{e}_p \cdot \mathbf{G}_i}{|\mathbf{G}_i|^2}, \tag{9}$$

where k_{pi} and λ_{pi} are the Bragg-matched wavenumber and wavelength for a grating component $\mathbf{G}_i$, respectively. Note that image degradation due to Bragg degeneracy will not occur in the PCR method because the Bragg-matched wavelength λ_{pi} is uniquely determined by the set of ($\mathbf{e}_p$, $\mathbf{G}_i$). In this case, the diffracted waves are reproduced with the direction vector

$$\mathbf{e}_{di} = \mathbf{e}_p + \mu_i \mathbf{G}_i . \tag{10}$$

The characteristic feature of the PCR method is that the wavelength of each diffracted plane wave is different at different grating components $\mathbf{G}_i$. Therefore, the PCR method can be applied only to Fourier holograms, where one grating vector corresponds to one particular point on the object plane. Even though all diffracted waves are obtained in an image hologram and a Fresnel hologram with polychromatic light, the image cannot be reconstructed since waves with different wavelengths cannot construct a point image.
An example of the reconstructed image in the PCR method is presented in Fig. 4, where we calculated the wavelength ratio μ_i and the direction vector $\mathbf{e}_{di}$ for each grating component $\mathbf{G}_i$ by using Eqs. (9) and (10), neglecting off-Bragg diffraction. In this simulation, we assumed

that the input image, which was an outline character "A" with dimensions 1 cm × 1 cm, shown in Fig. 4(a), was recorded at $\lambda_w = 532$ nm and was reconstructed with a polychromatic probe beam with a central wavelength λ_{p0} of 815 nm. From the figure, we can see that the reconstructed image was formed with spectral components ranging from 795 nm to 835 nm, and image magnification occurred in the y_d-direction. Such features are considered as a consequence of using the polychromatic light for the holographic reconstruction. In the following section, we will develop a theory of holographic reconstruction with polychromatic light and investigate characteristic features of the PCR method especially in holographic memory systems.

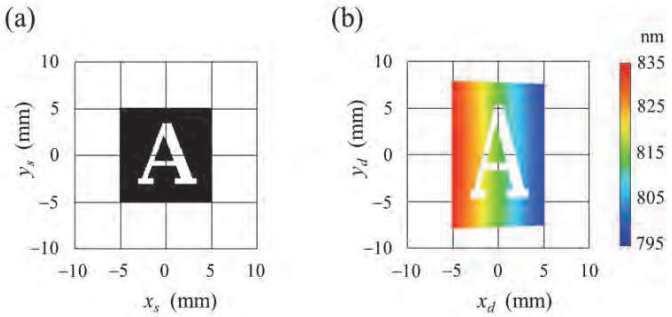

Fig. 4. Simulated results of image reconstruction by PCR. (a) Input image and (b) the reconstructed image. The color in (b) represents the Bragg-matched wavelength of each diffracted wave. The calculation parameters are as follows: $\lambda_w = 532$ nm; $\theta_w = 30°$; $\theta_p = 50°$; $n = 1$; and $f_s = f_d = 100$ mm.

3. Theory of holographic reconstruction with polychromatic light

3.1 Definition of the coordinate system

In this section, we introduce a coordinate system that allows for a more quantitative discussion of the PCR method. A Cartesian coordinate system is defined here using unit direction vectors $\mathbf{e}_{s0}$ and $\mathbf{e}_r$, as shown in Fig. 5(a), whose normal bases are given by

$$\mathbf{e}_x = \frac{\mathbf{e}_{s0} - \mathbf{e}_r}{\left|\mathbf{e}_{s0} - \mathbf{e}_r\right|},\ \mathbf{e}_y = -\frac{\mathbf{e}_{s0} \times \mathbf{e}_r}{\left|\mathbf{e}_{s0} \times \mathbf{e}_r\right|},\ \mathbf{e}_z = \frac{\mathbf{e}_{s0} + \mathbf{e}_r}{\left|\mathbf{e}_{s0} + \mathbf{e}_r\right|},\quad \left(\mathbf{e}_{s0} \neq \pm \mathbf{e}_r\right) \tag{11}$$

We introduce an elevation angle α_k and azimuthal angle β_k to specify a unit direction vector $\mathbf{e}_k$, as is depicted in Fig. 5(b). In this case the Cartesian components of $\mathbf{e}_k$ are written as

$$\mathbf{e}_k = \begin{bmatrix} e_{kx} \\ e_{ky} \\ e_{kz} \end{bmatrix} = \begin{bmatrix} \cos\alpha_k \sin\beta_k \\ \sin\alpha_k \\ \cos\alpha_k \cos\beta_k \end{bmatrix}. \qquad \left(k = si, r, p, di\right) \tag{12}$$

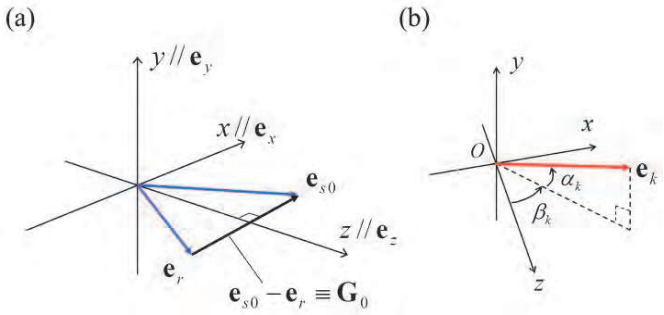

Fig. 5. Definition of (a) the Cartesian coordinate system and (b) the elevation angle α_k and the azimuthal angle β_k of the unit direction vector $\mathbf{e}_k$.

From the symmetry of the coordinate system and the Bragg condition of Eq. (5), the relations $\alpha_{s0} = 0$, $\alpha_r = 0$, $\beta_r = -\beta_{s0}$, and $\beta_{d0} = -\beta_p$ should hold. Thus, the direction vectors are written as

$$\mathbf{e}_{s0} = \begin{bmatrix} \sin\beta_{s0} \\ 0 \\ \cos\beta_{s0} \end{bmatrix}, \quad \mathbf{e}_r = \begin{bmatrix} -\sin\beta_{s0} \\ 0 \\ \cos\beta_{s0} \end{bmatrix}, \quad \mathbf{e}_p = \begin{bmatrix} \cos\alpha_p \sin\beta_p \\ \sin\alpha_p \\ \cos\alpha_p \cos\beta_p \end{bmatrix}, \quad \mathbf{e}_{d0} = \begin{bmatrix} -\cos\alpha_p \sin\beta_p \\ \sin\alpha_p \\ \cos\alpha_p \cos\beta_p \end{bmatrix},$$
$$\mathbf{G}_0 \equiv \mathbf{e}_{s0} - \mathbf{e}_r = \begin{bmatrix} 2\sin\beta_{s0} \\ 0 \\ 0 \end{bmatrix}. \qquad (0 < \beta_{s0} < \pi/2) \tag{13}$$

Note that if the grating component $\mathbf{G}_0$ and the wavelength ratio μ_0 are given, then $\mathbf{e}_p$ and $\mathbf{e}_{d0}$ have only one free parameter. This is because, from Eq. (5), α_p and β_p should satisfy

$$\cos\alpha_p \sin\beta_p = -\mu_0 \sin\beta_{s0}. \tag{14}$$

Furthermore, we express α_{si}, β_{si}, α_{di}, and β_{di}, as $\alpha_{si} = \alpha_{s0} + \delta\alpha_{si}$, $\beta_{si} = \beta_{s0} + \delta\beta_{si}$, $\alpha_{di} = \alpha_{d0} + \delta\alpha_{di}$, and $\beta_{di} = \beta_{d0} + \delta\beta_{di}$, respectively, and hereafter for simplicity, we assume that the divergence angles of the signal and diffracted beams are sufficiently small (i.e., $\delta\alpha_{si}$, $\delta\beta_{si}$, $\delta\alpha_{di}$, $\delta\beta_{di} \ll 1$) and the relations $|\boldsymbol{\delta}\mathbf{e}_{si}|^2$, $|\boldsymbol{\delta}\mathbf{e}_{di}|^2 \ll 1$ hold at all components i. Then, the deviation vectors $\boldsymbol{\delta}\mathbf{e}_{si}$ and $\boldsymbol{\delta}\mathbf{e}_{di}$ are approximated by

$$\boldsymbol{\delta}\mathbf{e}_{si} \equiv \mathbf{e}_{si} - \mathbf{e}_{s0} \approx \delta\alpha_{si} \begin{bmatrix} 0 \\ 1 \\ 0 \end{bmatrix} + \delta\beta_{si} \begin{bmatrix} \cos\beta_{s0} \\ 0 \\ -\sin\beta_{s0} \end{bmatrix} \equiv \delta\alpha_{si}\mathbf{e}_{s\alpha} + \delta\beta_{si}\mathbf{e}_{s\beta},$$
$$\boldsymbol{\delta}\mathbf{e}_{di} \equiv \mathbf{e}_{di} - \mathbf{e}_{d0} \approx \delta\alpha_{di} \begin{bmatrix} \sin\alpha_p \sin\beta_p \\ \cos\alpha_p \\ -\sin\alpha_p \cos\beta_p \end{bmatrix} + \cos\alpha_p \delta\beta_{di} \begin{bmatrix} \cos\beta_p \\ 0 \\ \sin\beta_p \end{bmatrix} \tag{15}$$
$$\equiv \delta\alpha_{di}\mathbf{e}_{d\alpha} + \cos\alpha_p \delta\beta_{di}\mathbf{e}_{d\beta},$$

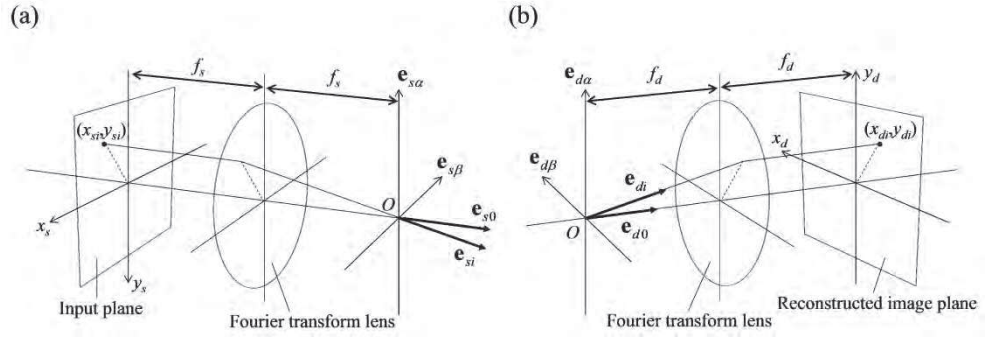

Fig. 6. The relation between the angular spectral component and the imaging position in the Fourier hologram. (a) The recording process and (b) the reconstruction process.

Note that the unit direction vectors $\mathbf{e}_{s\alpha}$ and $\mathbf{e}_{s\beta}$ correspond to the normal bases at the Fourier plane of the input image, as shown in Fig. 6(a). Thus, the position on the input plane (x_{si}, y_{si}) and the set of the deviation angles ($\delta\alpha_{si}$, $\delta\beta_{si}$) are related via

$$\begin{pmatrix} \delta\beta_{si} \\ \delta\alpha_{si} \end{pmatrix} = \frac{1}{f_s}\begin{pmatrix} x_{si} \\ y_{si} \end{pmatrix}, \tag{16}$$

where f_s is the focal length of the Fourier transform lens in the recording process. Similarly, the relation between the position on the reconstructed image plane (x_{di}, y_{di}) and the set of the deviation angles ($\delta\alpha_{di}$, $\delta\beta_{di}$) is given by

$$\begin{pmatrix} x_{di} \\ y_{di} \end{pmatrix} = f_d\begin{pmatrix} \cos\alpha_p\delta\beta_{di} \\ \delta\alpha_{di} \end{pmatrix}, \tag{17}$$

where f_d is the focal length of the Fourier transform lens in the reconstruction process. Furthermore, hereafter we assumed that the dimensions of the input image are in the ranges $-x_{sMax} \le x_{si} \le x_{sMax}$ and $-y_{sMax} \le y_{si} \le y_{sMax}$. Therefore, the maximum deviation angles of the signal beam, $\delta\alpha_{sMax}$ and $\delta\beta_{sMax}$, are

$$\begin{pmatrix} \delta\beta_{sMax} \\ \delta\alpha_{sMax} \end{pmatrix} = \frac{1}{f_s}\begin{pmatrix} x_{sMax} \\ y_{sMax} \end{pmatrix}. \tag{18}$$

3.2 Spectral width required for the reconstruction

In order to reconstruct the image information, an adequate spectral width is needed for the probe beam to satisfy the Bragg condition at every grating component. In this section, we will theoretically estimate such a spectral width. When we rewrite Eq. (9) using the deviation vectors $\boldsymbol{\delta}\mathbf{e}_{si}$, the difference between μ_i and μ_0 is given by

$$\delta\mu_i \equiv \mu_i - \mu_0 \approx -\frac{2\mathbf{e}_{d0}\cdot\boldsymbol{\delta}\mathbf{e}_{si}}{|\mathbf{G}_0|^2}, \tag{19}$$

where we assume that the relation $|\boldsymbol{\delta}\mathbf{e}_{si}|^2 << |\mathbf{G}_0|^2$ holds. Equation (19) indicates that the Bragg-matched wavelength does not depend only on the amplitude $|\boldsymbol{\delta}\mathbf{e}_{si}|$, but is determined by the projection of $\boldsymbol{\delta}\mathbf{e}_{si}$ on $\mathbf{e}_{d0}$. If we rewrite Eq. (19) using the Cartesian components in Eqs. (13) and (15) and the relation of Eq. (14), we obtain

$$\begin{aligned}\delta\mu_i &= -\frac{\sin\alpha_p\delta\alpha_{si} - \cos\alpha_p \sin\left(\beta_{s0}+\beta_p\right)\delta\beta_{si}}{2\sin^2\beta_{s0}} \\ &= \frac{\mu_0}{2}\left[\frac{\tan\alpha_p}{\sin\beta_{s0}\sin\beta_p}\delta\alpha_{si} - \left(\frac{1}{\tan\beta_{s0}}+\frac{1}{\tan\beta_p}\right)\delta\beta_{si}\right].\end{aligned} \tag{20}$$

Therefore, the spectral width required for the full image reconstruction ($\Delta\lambda_{BM}$) is given by

$$\Delta\lambda_{BM} = \lambda_{p0}\left[\frac{\tan|\alpha_p|}{\sin\beta_{s0}\sin\left(-\beta_p\right)}\frac{\delta y_{sMax}}{f_s} + \left(\frac{1}{\tan\beta_{s0}}+\frac{1}{\tan\beta_p}\right)\frac{\delta x_{sMax}}{f_s}\right]. \tag{21}$$

The Bragg-matched wavelength generally depends on both deviation angles $\delta\alpha_{si}$ and $\delta\beta_{si}$. When $\mathbf{e}_p$ lies in the xz-plane (i.e., $\alpha_p = 0°$), however, $\delta\mu_i$ depends only on the azimuthal deviation angle $\delta\beta_{si}$. To see these features more clearly, the spatial distributions of the Bragg-matched wavelength are illustrated in Fig. 7. In this simulation, we calculated the reconstructed image with the Bragg-matched wavelength assuming that the grating recorded at 532 nm was read out at around 815 nm. As is predicted from Eq. (21), the spectral width required for the probe beam has a minimum at $\alpha_p = 0°$. Furthermore, the distortion of the reconstructed image is also smallest at $\alpha_p = 0°$, which will be treated further in Section 3.3.

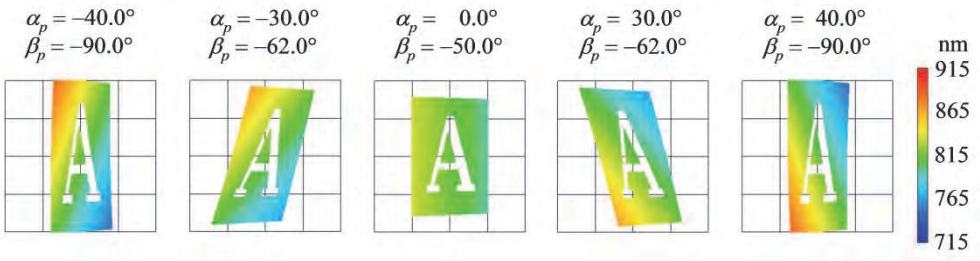

Fig. 7. The reconstructed images in the PCR method at several probe elevation angles α_p. The input image was the same as that in Fig. 4. The calculation parameters were as follows: $\lambda_w = 532$ nm; $\lambda_{p0} = 815$ nm; $\beta_{s0} = 30°$; $n = 1$; $f_s = f_d = 100$ mm; and β_p is determined from Eq. (14) at each α_p.

Rewriting Eq. (20) using the relation of Eq. (14) at the condition $\alpha_p = 0°$ yields

$$\delta\mu_i = -\frac{\mu_0}{2}\left\{\frac{1}{\tan\beta_{s0}} + \frac{1}{\tan\left[\arcsin\left(-\mu_0\sin\beta_{s0}\right)\right]}\right\}\delta\beta_{si}. \tag{22}$$

There is an optimum recording angle β_{s0Opt} that minimizes the required spectral width for a given μ_0, as shown in Fig. 8, which is given by

$$\beta_{s0Opt} = \arctan\left(\frac{1}{\mu_0}\right), \quad (\mu_0 \neq 1) \tag{23}$$

Then, Eq. (22) can be simplified to

$$\delta\mu_i = -\frac{1}{2}\left(\mu_0{}^2 - 1\right)\delta\beta_{si}\,. \tag{24}$$

In this case, the required spectral width $\Delta\lambda_{BM}$ reaches a minimum and is expressed as

$$\Delta\lambda_{BMMin} = \lambda_{p0}\left(\mu_0 - \frac{1}{\mu_0}\right)\frac{\delta x_{sMax}}{f_s}. \tag{25}$$

However, in most cases, the allowed deviation angle $\delta\beta_{sMax}$ is determined by the spectral width $\Delta\lambda_p$ of a given probe light source. Assuming that $\alpha_p = 0°$, from Eqs. (21), we obtain

$$\delta\beta_{s\max} = \left(\frac{1}{\tan\beta_{s0}} + \frac{1}{\tan\beta_p}\right)^{-1}\frac{\Delta\lambda_p}{\lambda_{p0}} \tag{26}$$

At the optimum recording angle, $\delta\beta_{sMax}$ reaches a maximum

$$\delta\beta_{sM\mathrm{ax}} = \left(\mu_0 - \frac{1}{\mu_0}\right)^{-1}\frac{\Delta\lambda_p}{\lambda_{p0}} \tag{27}$$

For example, if we have a probe light source whose central wavelength λ_{p0} is 815 nm and whose full spectral width $\Delta\lambda_p$ is 50 nm, and the recording wavelength λ_w is 532 nm, then the optimum recording angle β_{s0Opt} is about 33°, and the allowed deviation angle $\delta\beta_{sMax}$ is about 4.0°.

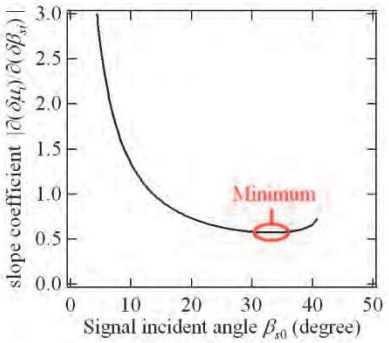

Fig. 8. The slope coefficient of $\delta\beta_{si}$ in Eq. (22) is plotted as a function of the signal incident angle β_{s0}. We assumed that $\lambda_w = 532$ nm and $\lambda_{p0} = 815$ nm.

So far, assuming the small deviation angles of the signal beam, we derived the expression for the Bragg-matched wavelength and found that the wavelength shift is simply proportional to the deviation angles $\delta\alpha_{si}$ and $\delta\beta_{si}$. However, for large deviation angles, their relation cannot be expressed by Eq. (20) and becomes nonlinear. Examples for the reconstructed images at large deviation angles are shown in Fig. 9. In this simulation, the focal length of the Fourier transform lenses was varied from 50 mm to 10 mm while the input image size was kept constant, which resulted in an increase of the maximum deviation angle from 5.7° to 30°. A larger angular spectrum of the signal beam results in greater deviation from the linear relationship and requires a probe beam of much broader spectrum. Moreover, considerable distortion of the reconstructed image occurs at large deviation angle.

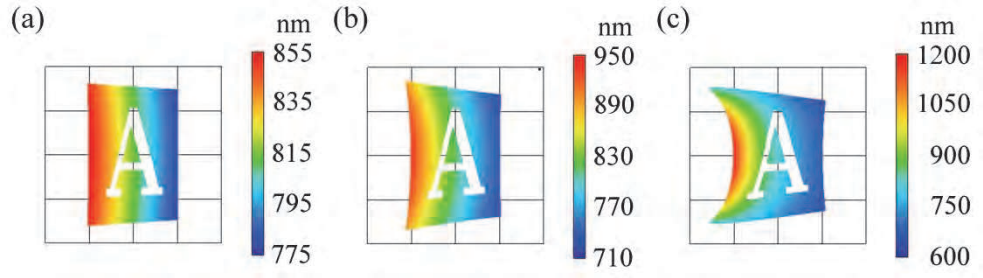

Fig. 9. Influence of large deviation angles $\delta\alpha_{si}$ and $\delta\beta_{si}$ on the reconstructed image. The input image was the same as that in Fig. 4. The focal lengths of the Fourier transform lenses are (a) $f_s = f_d = 50$ mm, (b) $f_s = f_d = 20$ mm, (c) $f_s = f_d = 10$ mm. The calculation parameters were as follows: $\lambda_w = 532$ nm; $\lambda_{p0} = 815$ nm; $\beta_{s0} = 30°$; and $n = 1$;

3.3 Distortion of the reconstructed image

In a thin hologram, it is well-known that magnification or reduction of the reconstructed image occurs during readout at a wavelength different from the recording one (Champagne, 1967). The PCR method, in contrast, produces a directionally-stretched image depending on the readout configuration, as shown in Fig. 7. Such distortion is likely to cause errors in retrieving data from volume holograms, but if the property of the distortion is known and predictable, the stored information can be completely recovered after the image processing of the distorted image. In this section, we will derive an expression for the distortion of the reconstructed image in the PCR method.

From Eq. (10), the deviation vector $\boldsymbol{\delta}\mathbf{e}_{di}$ is approximated by

$$\boldsymbol{\delta}\mathbf{e}_{di} \equiv \mathbf{e}_{di} - \mathbf{e}_{d0} \approx \mu_0 \boldsymbol{\delta}\mathbf{e}_{si} + \delta\mu_i \mathbf{G}_0 , \tag{28}$$

where we neglect the product of $\boldsymbol{\delta}\mathbf{e}_{si}$ and $\delta\mu_0$. From Eqs. (13), (15), and (20), the Cartesian components of $\boldsymbol{\delta}\mathbf{e}_{di}$ are expressed as

$$\boldsymbol{\delta}\mathbf{e}_{di} = \mu_0 \begin{bmatrix} \cos\beta_{s0}\delta\beta_{si} \\ \delta\alpha_{si} \\ -\sin\beta_{s0}\delta\beta_{si} \end{bmatrix} - \frac{\sin\alpha_p \delta\alpha_{si} - \cos\alpha_p \sin\left(\beta_{s0}+\beta_p\right)\delta\beta_{si}}{2\sin^2\beta_{s0}} \begin{bmatrix} 2\sin\beta_{s0} \\ 0 \\ 0 \end{bmatrix}. \tag{29}$$

On the other hand, $\boldsymbol{\delta}\mathbf{e}_{di}$ is also expressed by Eq. (15) using $\mathbf{e}_{d\alpha}$ and $\mathbf{e}_{d\beta}$. Rewriting Eq. (29) using normal bases of $\mathbf{e}_{d\alpha}$ and $\mathbf{e}_{d\beta}$ yields

$$\boldsymbol{\delta}\mathbf{e}_{di} = \left(\frac{\mu_0}{\cos\alpha_p} \delta\alpha_{si} \right) \mathbf{e}_{d\alpha} + \left(\mu_0 \frac{\tan\alpha_p}{\tan\beta_p} \delta\alpha_{si} + \cos\alpha_p \delta\beta_{si} \right) \mathbf{e}_{d\beta} . \tag{30}$$

Comparing the coefficients in (30) with those in Eq. (15), we obtain the relation between the deviation angles ($\delta\alpha_{si}$, $\delta\beta_{si}$) and ($\delta\alpha_{di}$, $\delta\beta_{di}$):

$$\begin{pmatrix} \cos\alpha_p \delta\beta_{di} \\ \delta\alpha_{di} \end{pmatrix} = \begin{pmatrix} \cos\alpha_p & \mu_0 \dfrac{\tan\alpha_p}{\tan\beta_p} \\ 0 & \dfrac{\mu_0}{\cos\alpha_p} \end{pmatrix} \begin{pmatrix} \delta\beta_{si} \\ \delta\alpha_{si} \end{pmatrix}. \tag{31}$$

From Eqs. (16) and (17), we can finally derive the expression for a transfer matrix between the object and reconstructed image plane, that is,

$$\begin{pmatrix} x_{di} \\ y_{di} \end{pmatrix} = \mathbf{T} \begin{pmatrix} x_{si} \\ y_{si} \end{pmatrix}, \quad \mathbf{T} \equiv \frac{f_d}{f_s} \begin{pmatrix} \cos\alpha_p & \mu_0 \dfrac{\tan\alpha_p}{\tan\beta_p} \\ 0 & \dfrac{\mu_0}{\cos\alpha_p} \end{pmatrix}. \tag{32}$$

When $\alpha_p = 0°$ or $\beta_p = -90°$, non-diagonal components in the transfer matrix become zero and the image can be reconstructed without any tilting. However, the distortion becomes minimal at $\alpha_p = 0°$, as was seen in Fig. 7.

3.4 Multiplexing with crystal rotation

In this section, we investigate the multiplexing capability in the PCR method. While many multiplexing methods have been proposed so far, we adopt peristrophic multiplexing (Curtis et al., 1994) and rotation of the crystal angle (hereafter, the latter will be called crystal angle multiplexing). The multiplexing configuration considered here is shown in Fig. 10. Note that other multiplexing methods are also possible in principle, but most of them are probably not suitable for the PCR method because they require a complicated system to read a target page. For example, ordinary angle multiplexing, which varies the incident angle of the reference beam, will also require moving the imaging system. This is because $\mathbf{e}_{d0}$ will be pointed in a different direction at each multiplexed page, as expressed by Eq. (10). The situation is similar in the case of the wavelength multiplexing method. Peristrophic multiplexing and crystal angle multiplexing, in contrast, do not require any additional movement other than the crystal rotation. In addition, the imaging properties are almost unchanged with each multiplexed page because the recording angle is constant. Thus, these multiplexing methods are suitable for holographic memory systems employing PCR.

In the peristrophic and crystal angle multiplexing methods, recording of another page is performed after crystal rotation by the proper angle. In order to retrieve the stored information without crosstalk, the rotation angle should be sufficiently large so that the other multiplexed holograms cannot produce noise diffracted waves that would disturb the detection of the target

signal image. On the other hand, the theoretical limit of the storage density is inversely proportional to the angular separation between the adjacent multiplexed holograms. Therefore, the angular selectivity (i.e., how small the angular separation can be made) is an important figure of merit determining the total storage density of the system. In the following sections, we will derive an expression of the minimum rotation angle for each multiplexing method.

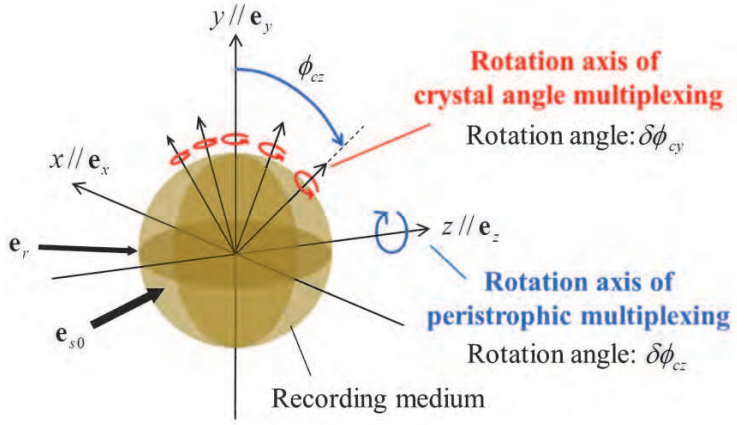

Fig. 10. Configuration of crystal angle multiplexing combined with peristrophic rotation. Peristrophic multiplexing and crystal angle multiplexing are performed by rotating the crystal around the z-axis and an axis inclined at ϕ_{cz} from the *y*-axis, respectively.

3.4.1 Peristrophic multiplexing

When the crystal is rotated by a small angle $\delta\phi_{cz}$ around the *z*-axis (peristrophic rotation), the displacement vector of the grating component ($\boldsymbol{\delta}\mathbf{e}_{cz}$) is approximated by

$$\boldsymbol{\delta}\mathbf{e}_{cz} \equiv \begin{pmatrix} 1 & -\delta\phi_{cz} & 0 \\ \delta\phi_{cz} & 1 & 0 \\ 0 & 0 & 1 \end{pmatrix} \mathbf{G}_i - \mathbf{G}_i \approx \begin{bmatrix} 0 \\ 2\sin\beta_{s0}\delta\phi_{cz} \\ 0 \end{bmatrix}. \tag{33}$$

Note that we neglected the product of small quantities. Due to the small rotation of the grating vectors, the Bragg-matched wavelength and the unit direction vector of each diffracted wave are also changed according to Eqs. (9) and (10). The shift of the wavelength ratio after the peristrophic rotation ($\delta\mu_{cz}$) is given by

$$\begin{aligned} \delta\mu_{cz} &\equiv -\frac{2\mathbf{e}_p \cdot (\mathbf{G}_i + \boldsymbol{\delta}\mathbf{e}_{cz})}{|\mathbf{G}_i + \boldsymbol{\delta}\mathbf{e}_{cz}|^2} - \left(-\frac{2\mathbf{e}_p \cdot \mathbf{G}_i}{|\mathbf{G}_i|^2} \right) \\ &\approx -\frac{2\mathbf{e}_{d0} \cdot \boldsymbol{\delta}\mathbf{e}_{cz}}{|\mathbf{G}_0|^2} \\ &= -\frac{\sin\alpha_p}{\sin\beta_{s0}} \delta\phi_{cz}, \end{aligned} \tag{34}$$

where last equality is obtained by substituting Eqs. (13) and (33). The displacement vector of $\mathbf{e}_{di}$ after the peristrophic rotation ($\boldsymbol{\delta}\mathbf{e}_{dcz}$) is expressed as

$$\begin{aligned}\boldsymbol{\delta}\mathbf{e}_{dcz} &\equiv \left[\mathbf{e}_p + (\mu_i + \delta\mu_{cz})(\mathbf{G}_i + \boldsymbol{\delta}\mathbf{e}_{cz})\right] - (\mathbf{e}_p + \mu_i\mathbf{G}_i) \\ &\approx \mu_0\boldsymbol{\delta}\mathbf{e}_{cz} + \delta\mu_{cz}\mathbf{G}_0 \\ &= -2\delta\phi_{cz}\begin{bmatrix}\sin\alpha_p \\ \cos\alpha_p \sin\beta_p \\ 0\end{bmatrix},\end{aligned} \tag{35}$$

where we use Eqs. (13), (14), (33), and (34) to derive the last equality. If we rewrite Eq. (35) using normal bases of $\mathbf{e}_{d\alpha}$ and $\mathbf{e}_{d\beta}$ and compare the coefficients with those in Eq. (15), similarly to Section 3.3, we obtain the shift amount of the imaging position due to the peristrophic rotation:

$$\begin{pmatrix}\delta x_{dicz} \\ \delta y_{dicz}\end{pmatrix} = 2\mu_0 \sin\beta_{s0} f_d \begin{pmatrix}\dfrac{\tan\alpha_p}{\tan\beta_p} \\ \dfrac{1}{\cos\alpha_p}\end{pmatrix}\delta\phi_{cz}. \tag{36}$$

For simplicity, we assume that $\alpha_p = 0$. Then, from Eqs. (20), (32), (34), and (36), the Bragg-matched wavelength λ_{BMcz} can be expressed as a function of the imaging position (x_d, y_d) and the rotation angle $\delta\phi_{cz}$:

$$\begin{aligned}&\lambda_{BMcz}(x_d, y_d, \delta\phi_{cz}) \approx \lambda_{p0} - \frac{\lambda_{p0}}{2}\left(\frac{1}{\tan\beta_{s0}} + \frac{1}{\tan\beta_p}\right)\frac{x_d}{f_d} \\ &\begin{pmatrix} -x_{sMax}\dfrac{f_d}{f_s} \le x_d \le x_{sMax}\dfrac{f_d}{f_s} \\ -\mu_0 y_{sMax}\dfrac{f_d}{f_s} + 2\mu_0\sin\beta_{s0} f_d\delta\phi_{cz} \le y_d \le \mu_0 y_{sMax}\dfrac{f_d}{f_s} + 2\mu_0\sin\beta_{s0} f_d\delta\phi_{cz}\end{pmatrix}.\end{aligned} \tag{37}$$

Note that the inequality in Eq. (37) represents the location of the reconstructed image. The peristrophic rotation causes the reconstructed image to shift in the y_d direction while keeping the spatial distribution of the Bragg-matched wavelength unchanged. In order to record another page without crosstalk, the rotation angle should be large enough to shift the noise image away from the signal imaging area. Thus, from the inequality in Eq. (37), the minimum angular separation in peristrophic multiplexing ($\delta\phi_{czMin}$) is expressed as

$$\delta\phi_{czMin} = \frac{y_{sMax}}{\sin\beta_{s0} f_s}. \tag{38}$$

This equation does not include the wavelength ratio μ_0. Therefore, the readout at a longer wavelength does not affect the angular selectivity in the peristrophic multiplexing, even though the reconstructed image was magnified by a factor of μ_0 in the y_d direction. This is because the amount of spatial shift is also increased by a factor of μ_0, as shown in Eq. (36).

In order to see these behaviours more clearly, in Fig. 11, we show the simulated results of the reconstructed image obtained while varying the peristrophic rotation angle $\delta\phi_{cz}$. We also present results for the conventional monochromatic readout for comparison. Note that the off-Bragg diffraction was also neglected in the monochromatic case, but here, in order to see the influence of the peristrophic rotation on the Bragg condition, the probe light was assumed to be quasi-monochromatic with a small spectral width of 1 nm, instead of taking the finite hologram dimension into account. Although a part of the image faded away due to the Bragg selectivity in the quasi-monochromatic case, the rotation angles required for multiplexing are almost the same in both cases. Therefore, the use of polychromatic light in the PCR method has only a small influence on the multiplexing capability in the peristrophic multiplexing method, and the PCR method could employ peristrophic multiplexing without any adverse influence on the multiplexing capability.

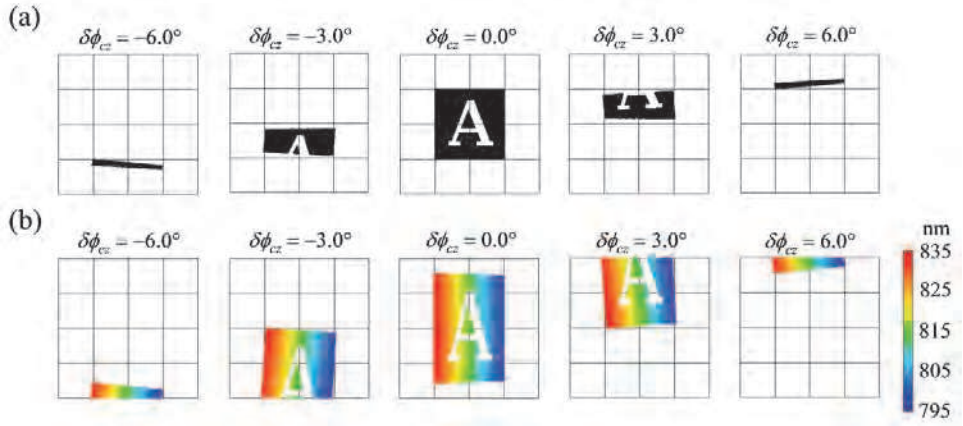

Fig. 11. Influence of the peristrophic rotation on the reconstructed image obtained with (a) conventional quasi-monochromatic light whose central wavelength is 532 nm and whose spectral width is 1 nm, and (b) polychromatic light whose central wavelength is 815 nm and whose spectral width is 40 nm. $\delta\phi_{cz}$ is the peristrophic rotation angle.

3.4.2 Crystal angle multiplexing with peristrophic rotation

Next, let us consider the angular selectivity in the crystal angle multiplexing, where the crystal is rotated around an axis inclined at ϕ_{cz}, as shown in Fig. 10. Note that the inclination angle ϕ_{cz} results from the crystal rotation due to the peristrophic multiplexing. In a similar way to the previous section, the displacement vector $\mathbf{G}_i$ due to a small rotation in the crystal angle multiplexing ($\boldsymbol{\delta}\mathbf{e}_{cy}$) is approximated by

$$\boldsymbol{\delta}\mathbf{e}_{cy} \equiv \begin{pmatrix} 1 & 0 & \cos\phi_{cz}\delta\phi_{cy} \\ 0 & 1 & \sin\phi_{cz}\delta\phi_{cy} \\ -\cos\phi_{cz}\delta\phi_{cy} & -\sin\phi_{cz}\delta\phi_{cy} & 1 \end{pmatrix} \mathbf{G}_i - \mathbf{G}_i \approx \begin{bmatrix} 0 \\ 0 \\ -2\sin\beta_{s0}\cos\phi_{cz}\delta\phi_{cy} \end{bmatrix}. \quad (39)$$

In this case, the shift of the wavelength ratio ($\delta\mu_{cy}$) and the displacement vector of $\mathbf{e}_{di}$ after the crystal rotation ($\boldsymbol{\delta}\mathbf{e}_{dcy}$) are expressed as

$$\delta\mu_{cy} \approx -\frac{2\mathbf{e}_{d0}\cdot\boldsymbol{\delta}\mathbf{e}_{cy}}{\left|\mathbf{G}_0\right|^2} = \frac{\cos\alpha_p\cos\beta_p}{\sin\beta_{s0}}\cos\phi_{cz}\delta\phi_{cy} \tag{40}$$

and

$$\boldsymbol{\delta}\mathbf{e}_{dcy} \approx \mu_0\boldsymbol{\delta}\mathbf{e}_{cy} + \delta\mu_{cy}\mathbf{G}_0 = 2\cos\alpha_p\cos\varphi_{cz}\delta\phi_{cy}\begin{bmatrix}\cos\beta_p\\0\\\sin\beta_p\end{bmatrix}, \tag{41}$$

respectively. Then, the imaging shift due to the rotation of the crystal angle multiplexing is written as

$$\begin{pmatrix}\delta x_{dicy}\\ \delta y_{dicy}\end{pmatrix} = f_d\begin{pmatrix}2\cos\alpha_p\cos\phi_{cz}\delta\phi_{cy}\\0\end{pmatrix}. \tag{42}$$

Thus, the reconstructed image will shift in the x_d direction regardless of α_p. Assuming that $\alpha_p = 0$, we obtain the Bragg-matched wavelength λ_{BMcy} as a function of the imaging position (x_d, y_d) and the rotation angles $\delta\phi_{cy}$ and ϕ_{cz}:

$$\lambda_{BMcy}\left(x_d, y_d, \delta\phi_{cy}, \phi_{cz}\right) \approx \lambda_{p0} - \frac{\lambda_{p0}}{2}\left(\frac{1}{\tan\beta_{s0}} + \frac{1}{\tan\beta_p}\right)\frac{x_d}{f_d} + \frac{\lambda_{p0}}{\tan\beta_{s0}}\cos\phi_{cz}\delta\phi_{cy}$$
$$\left(\begin{array}{c}-x_{sMax}\dfrac{f_d}{f_s} + 2f_d\cos\phi_{cz}\delta\phi_{cy} \le x_d \le x_{sMax}\dfrac{f_d}{f_s} + 2f_d\cos\phi_{cz}\delta\phi_{cy}\\ -\mu_0 y_{sMax}\dfrac{f_d}{f_s} \le y_d \le \mu_0 y_{sMax}\dfrac{f_d}{f_s}\end{array}\right). \tag{43}$$

In contrast to peristrophic multiplexing, the crystal angle multiplexing leads to a change in the Bragg-matched wavelength as well as a shift of the imaging location. The Bragg-matched wavelength in Eq. (43) is plotted at several rotation angles $\delta\phi_{cy}$ in Fig. 12. The dotted part of the Bragg-matched line in the figure corresponds to the portion of the image that is not reconstructed by the probe beam because the Bragg-matched wavelength is beyond the probe spectral band. Such behaviour can be clearly seen in Fig. 13.

When the solid part of the Bragg-matched line lies inside the signal imaging area, the noise diffraction will spatially overlap with the signal image and cause severe crosstalk. Therefore, the angular separation between adjacent holograms should be sufficiently large so that the solid part will be shifted away from the signal imaging area. If we assume that the central wavelength of the probe beam is λ_{p0} and its full spectral width is $\Delta\lambda_p$, the minimum angular separation ($\delta\phi_{cyMin}$) is given by

$$\delta\phi_{cyMin} = \min\left[\frac{x_{sMax}}{\cos\phi_{cz}f_s}, \frac{\tan\beta_{s0}}{2\cos\phi_{cz}\lambda_{p0}}\left(\Delta\lambda_p + \lambda_{p0}\left(\frac{1}{\tan\beta_{s0}} + \frac{1}{\tan\beta_p}\right)\frac{x_{sMax}}{f_s}\right)\right], \tag{44}$$

where min[*a*, *b*] is a minimum function yielding the smaller value of *a* and *b*. Note that the former parameter in the minimum function is the rotation angle required for separating the noise and signal images spatially, and the latter corresponds to that required for spectral separation. The above equation implies that an unnecessarily large spectral width increases the minimum angular separation needlessly. Thus, if we take the spectral width required for the full image reconstruction, $\Delta\lambda_{BM}$ in Eq. (25), as the probe spectral width $\Delta\lambda_p$, then $\delta\phi_{cyMin}$ is given by

$$\delta\phi_{cyMin} = \left(1 + \frac{\tan\beta_{s0}}{\tan\beta_p}\right)\frac{x_{sMax}}{\cos\phi_{cz} f_s}. \tag{45}$$

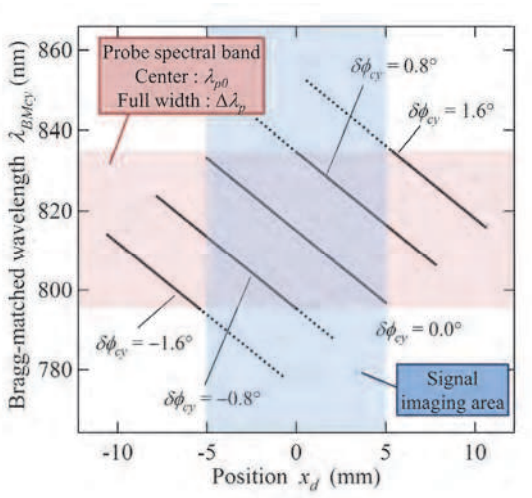

Fig. 12. The imaging location x_d and the Bragg-matched wavelength λ_{BMcy} at each rotation angle $\delta\phi_{cy}$. The reconstructed image field is limited by the probe spectral band $\Delta\lambda_p$. The dotted part of the Bragg-matched line corresponds to the portion of the image that will not be reconstructed by the probe beam. The peristrophic rotation angle ϕ_{cz} is assumed to be zero.

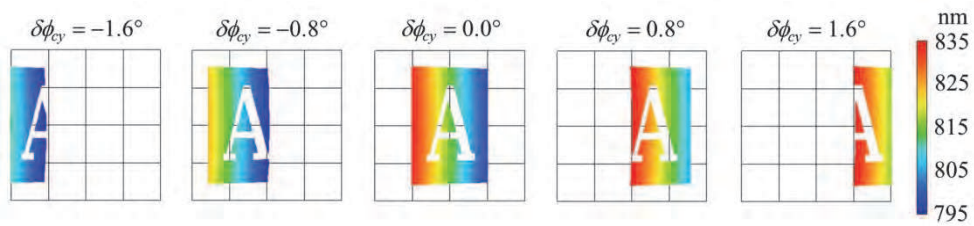

Fig. 13. The reconstructed images after the crystal rotation around the *y*-axis. $\delta\phi_{cy}$ is the rotation angle. The polychromatic light with a central wavelength of 815 nm and a spectral width of 40 nm was used.

Note that when the wavelength ratio μ_0 is unity (i.e., the readout wavelength is the same as the recording one), the required angular separation $\delta\phi_{cyMin}$ becomes zero. This is because we assumed that the hologram dimension is large enough to neglect off-Bragg diffraction. In other words, if we employ the PCR method, the angular separation specified by Eq. (45) is always required, regardless of the hologram dimension.

3.5 Off-Brag diffraction

So far, we considered only the diffracted wave satisfying the Bragg condition. In reality, however, owing to the finite hologram dimension, the grating produces non-Bragg-matched diffracted waves, referred to as off-Bragg diffraction. In this section, we consider the off-Brag diffraction in the PCR method and derive expressions for crosstalk noise.

We assume that a set of ($\mathbf{G}_i$, $\mathbf{e}_p$, $\mathbf{e}_{di}$) satisfies the Bragg condition at λ_w and λ_{pi} and consider the situation where a grating component $\mathbf{G}_i + \boldsymbol{\delta}\mathbf{e}_{Goff}$ produces a diffracted wave whose wavelength and unit direction vector are $\lambda_{pi} + \delta\lambda_{off}$ and $\mathbf{e}_{di}$, respectively. In this case, the off-Bragg vector $\boldsymbol{\Delta}\mathbf{K}$ can be written as

$$\boldsymbol{\Delta}\mathbf{K} \equiv k_w\left(\mathbf{G}_i + \boldsymbol{\delta}\mathbf{e}_{Goff}\right) - \frac{2\pi n_p}{\lambda_{pi} + \delta\lambda_{off}}\left(\mathbf{e}_{di} - \mathbf{e}_p\right) \approx k_w\left(\boldsymbol{\delta}\mathbf{e}_{Goff} + \frac{\delta\lambda_{off}}{\lambda_{p0}}\mathbf{G}_0\right), \tag{46}$$

where we also assumed that the relation $\delta\lambda_{off} << \lambda_{pi}$ holds. The grating deviation vector $\boldsymbol{\delta}\mathbf{e}_{Goff}$ can be divided into two classes according to the origin. One is related to the grating that is formed by a different signal component $\mathbf{e}_{si}$ + $\boldsymbol{\delta}\mathbf{e}_{soff}$. The other corresponds to the grating recorded in a different multiplexed page. Thus, $\boldsymbol{\delta}\mathbf{e}_{Goff}$ can be expressed as

$$\boldsymbol{\delta}\mathbf{e}_{Goff} = \boldsymbol{\delta}\mathbf{e}_{soff} + \boldsymbol{\delta}\mathbf{e}_{cy} + \boldsymbol{\delta}\mathbf{e}_{cz}\,, \tag{47}$$

where $\boldsymbol{\delta}\mathbf{e}_{cz}$ and $\boldsymbol{\delta}\mathbf{e}_{cy}$ are the displacement vectors due to the crystal rotation, defined by Eqs. (33) and (39), respectively. Then the Cartesian components of Eq. (46) can be written as

$$\begin{bmatrix}\Delta K_x\\ \Delta K_y\\ \Delta K_z\end{bmatrix} = k_w\begin{pmatrix}0 & \cos\beta_{s0} & 0 & 0 & 2\sin\beta_{s0}\\ 1 & 0 & 0 & 2\sin\beta_{s0} & 0\\ 0 & -\sin\beta_{s0} & -2\cos\phi_{cz}\sin\beta_{s0} & 0 & 0\end{pmatrix}\begin{bmatrix}\delta\alpha_{soff}\\ \delta\beta_{soff}\\ \delta\phi_{cy}\\ \delta\phi_{cz}\\ \delta\lambda_{off}/\lambda_{p0}\end{bmatrix}, \tag{48}$$

where $\delta\alpha_{soff}$ and $\delta\beta_{soff}$ are the off-Bragg deviation angles that are related to $\boldsymbol{\delta}\mathbf{e}_{soff}$ through Eq. (15). If we assume that the modulation of the grating is weak enough to validate the Born approximation, the intensity of the off-Bragg diffracted wave can be expressed as (Barbastathis & Psaltis, 2000)

$$I_{off} \propto \left[\operatorname{sinc}\left(\frac{\Delta K_x L_x}{2}\right)\cdot\operatorname{sinc}\left(\frac{\Delta K_y L_y}{2}\right)\cdot\operatorname{sinc}\left(\frac{\Delta K_z L_z}{2}\right)\right]^2 I_p\left(\lambda_{pi} + \delta\lambda_{off}\right)d\lambda\,, \tag{49}$$

where L_x, L_y, and L_z are the hologram dimensions in the x, y, and z directions, respectively;

$$\mathrm{sinc}(x) \equiv \frac{\sin(x)}{x} \tag{50}$$

is the sinc function;

$$I_p(\lambda) = \frac{I_{p0}}{\Delta\lambda_p}\,\mathrm{rect}\left(\frac{\lambda - \lambda_{p0}}{\Delta\lambda_p}\right), \tag{51}$$

is the spectral intensity of the probe beam whose central wavelength, full spectral width, and intensity are λ_{p0}, $\Delta\lambda_p$, and I_{p0}, respectively; and rect(x) is the rectangle function, defined as

$$\mathrm{rect}(x) = \begin{cases} 1 & |x| < 1/2 \\ 1/2 & |x| = 1/2 \\ 0 & |x| > 1/2 \end{cases}. \tag{52}$$

Equation (49) indicates that the off-Bragg diffraction will occur at $\mathbf{\Delta K}$ around the origin. The diffracted intensity will become zero when the relation

$$|\Delta K_i| = \frac{2\pi}{L_i} \quad (i = x, y, z) \tag{53}$$

holds at any component of the off-Bragg vector $\mathbf{\Delta K}$. Thus, hereafter, we assume that Eq. (53) represents an upper limit of $|\Delta K_i|$ in which the grating $\mathbf{G}_i + \mathbf{\delta e}_{Goff}$ can produce off-Bragg diffraction.

3.5.1 Properties of signal diffraction

Before considering the crosstalk noise, let us first discuss the prpperties of signal diffraction from a target grating $\mathbf{G}_i$. In this case, we can set $\delta\alpha_{soff} = \delta\beta_{soff} = \delta\phi_{cy} = \delta\phi_{cz} = 0°$. Then the off-Bragg vector in Eq. (48) can be simplified to

$$\begin{bmatrix} \Delta K_x \\ \Delta K_y \\ \Delta K_z \end{bmatrix} = k_w \begin{pmatrix} 2\sin\beta_{s0}\,\delta\lambda_{off}/\lambda_{p0} \\ 0 \\ 0 \end{pmatrix}. \tag{54}$$

From Eq. (49), the intensity of the signal diffracted wave at wavelength $\lambda_{pi} + \delta\lambda_{off}$ is written as

$$I_{off} \propto \mathrm{sinc}^2\left(\frac{\pi\delta\lambda_{off}}{\delta\lambda_{offMax}}\right) I_p\left(\lambda_{pi} + \delta\lambda_{off}\right) d\lambda, \tag{55}$$

where

$$\delta\lambda_{offMax} = \frac{\lambda_w \lambda_{p0}}{2n_w \sin\beta_{s0} L_x} \tag{56}$$

is the half spectral width of the signal diffracted wave. Therefore, a target grating $\mathbf{G}_i$ produces the signal diffraction with a certain spectral width which depends on the hologram dimension L_x. The total intensity of the signal diffracted wave (I_{dif}) can be calculated by integrating Eq. (55). The result is given by

$$I_{dif} \propto \int_{-\infty}^{\infty} \mathrm{sinc}^2\left(\frac{\pi\delta\lambda_{off}}{\delta\lambda_{offMax}}\right) I_p\left(\lambda_{pi}+\delta\lambda_{off}\right) d\left(\delta\lambda_{off}\right) \approx \frac{\delta\lambda_{offMax}}{\Delta\lambda_p} I_{p0}\,, \tag{57}$$

where we assumed that the probe spectral width $\Delta\lambda_p$ is much larger than $\delta\lambda_{offMax}$, meaning that $I_p(\lambda)$ is considered to be a constant over the region where the integrand is appreciable, and we used the relation

$$\int_{-\infty}^{\infty} \mathrm{sinc}^2\left(x\right) dx = \pi\,. \tag{58}$$

Note that if $\Delta\lambda_p \to 0$, then $I_{dif} \to I_{p0}$. Thus, the diffraction efficiency in the PCR method is a factor of $\delta\lambda_{offMax}/\Delta\lambda_p$ smaller than that in monochromatic readout. This is because the grating component $\mathbf{G}_i$ can diffract only the limited spectral component around λ_{pi}. Such a reduction in the diffraction efficiency is an unavoidable drawback of the PCR method.

3.5.2 Intra-page crosstalk noise

In this section, we will consider the intra-page crosstalk noise which is derived from the unwanted diffraction coming from the same page but a different grating component, $\mathbf{G}_i + \boldsymbol{\delta}\mathbf{e}_{soff}$. In this case, we can set $\delta\phi_{cy} = \delta\phi_{cz} = 0°$, and then the off-Bragg vector in Eq. (48) can be rewritten as

$$\begin{bmatrix}\Delta K_x\\ \Delta K_y\\ \Delta K_z\end{bmatrix} = k_w \begin{bmatrix}\cos\beta_{s0}\delta\beta_{soff} + 2\sin\beta_{s0}\,\delta\lambda_{off}/\lambda_{p0}\\ \delta\alpha_{soff}\\ -\sin\beta_{s0}\delta\beta_{soff}\end{bmatrix}. \tag{59}$$

The off-Bragg diffraction will occur only when a set of ($\delta\alpha_{soff}$, $\delta\lambda_{off}$) satisfies all of the following inequalities:

$$-\frac{\lambda_w}{n_w\cos\beta_{s0}L_x} \le \delta\beta_{soff} + 2\tan\beta_{s0}\frac{\delta\lambda_{off}}{\lambda_{p0}} \le \frac{\lambda_w}{n_w\cos\beta_{s0}L_x}\,, \tag{60}$$

$$-\frac{\lambda_w}{n_w L_y} \le \delta\alpha_{soff} \le \frac{\lambda_w}{n_w L_y}\,, \tag{61}$$

$$-\frac{\lambda_w}{n_w\sin\beta_{s0}L_z} \le \delta\beta_{soff} \le \frac{\lambda_w}{n_w\sin\beta_{s0}L_z}\,. \tag{62}$$

On the other hand, the variable ranges of $\delta\alpha_{soff}$, $\delta\beta_{soff}$, and $\delta\lambda_{off}$ are also restricted by the input image size or the probe spectrum, which are given by

$$\begin{aligned} &-\delta\alpha_{sMax} \le \delta\alpha_{si} + \delta\alpha_{soff} \le \delta\alpha_{sMax} \\ \Leftrightarrow\ &-\delta\alpha_{si} - \delta\alpha_{sMax} \le \delta\alpha_{soff} \le -\delta\alpha_{si} + \delta\alpha_{sMax} \end{aligned} \tag{63}$$

$$\begin{aligned} &-\delta\beta_{sMax} \le \delta\beta_{si} + \delta\beta_{soff} \le \delta\beta_{sMax} \\ \Leftrightarrow\ &-\delta\beta_{si} - \delta\beta_{sMax} \le \delta\beta_{soff} \le -\delta\beta_{si} + \delta\beta_{sMax} \end{aligned} \tag{64}$$

$$\begin{aligned} &\lambda_{p0} - \frac{\Delta\lambda_p}{2} \le \lambda_{p0} + \delta\lambda_{pi} + \delta\lambda_{off} \le \lambda_{p0} + \frac{\Delta\lambda_p}{2} \\ \Leftrightarrow\ &-\delta\lambda_{pi} - \frac{\Delta\lambda_p}{2} \le \delta\lambda_{off} \le -\delta\lambda_{pi} + \frac{\Delta\lambda_p}{2}, \end{aligned} \tag{65}$$

where $\delta\lambda_{pi}$ is the difference between λ_{pi} and λ_{p0}. Note that the above ranges depend on the targeting position (x_{si}, y_{si}) within the input image.

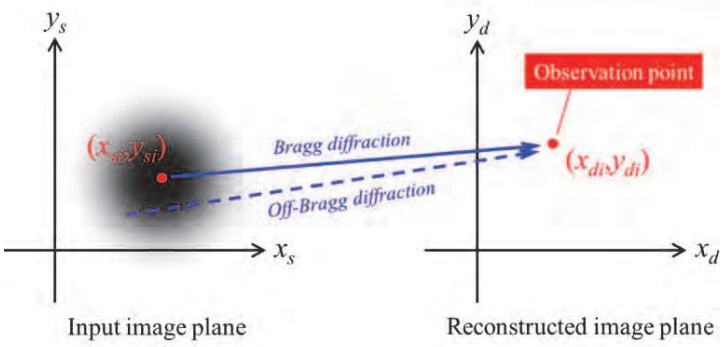

Fig. 14. Schematic diagram of the intra-page crosstalk noise. The off-Bragg diffracted waves coming from other input positions will reach the same position as the signal diffracted wave.

Our goal in this section is to find an upper limit of the off-Bragg deviation angles ($\delta\alpha_{soff}$, $\delta\beta_{soff}$). Such maximum angles specify an input image area suffering from intra-page crosstalk noise, as shown in Fig. 14. First, we will consider the conventional monochromatic case because it can be understood more easily. Since the probe beam is monochromatic, we can set $\delta\lambda_{off} = 0$. Then, the maximum off-Bragg deviation angles $\delta\alpha_{soffMax(mono)}$ and $\delta\beta_{soffMax(mono)}$ are obtained from Eqs. (60), (61), and (62):

$$\delta\alpha_{soffMax(mono)} = \frac{\lambda_w}{n_w L_y} \tag{66}$$

$$\delta\beta_{soffMax(mono)} = \min\left[\frac{\lambda_w}{n_w \cos\beta_{s0} L_x}, \frac{\lambda_w}{n_w \sin\beta_{s0} L_z}\right]. \tag{67}$$

Note that $\delta\alpha_{soffMax(mono)}$ and $\delta\beta_{soffMax(mono)}$ are usually much smaller than $\delta\alpha_{sMax}$ and $\delta\beta_{sMax}$ and satisfy Eqs. (63) and (64), respectively.

Next, we move to the polychromatic case. In this case, the variable range of $\delta\lambda_{off}$ is appreciable owing to the large spectral width $\Delta\lambda_p$, as expressed in Eq. (65). On the other hand, in order to satisfy Eqs. (60) and (62) at the same $\delta\beta_{soff}$, there should exist a common region in the two inequalities; that is,

$$\begin{cases} -\dfrac{\lambda_w}{n_w \sin\beta_{s0} L_z} \le -2\tan\beta_{s0}\dfrac{\delta\lambda_{off}}{\lambda_{p0}} + \dfrac{\lambda_w}{n_w \cos\beta_{s0} L_x} \\ -2\tan\beta_{s0}\dfrac{\delta\lambda_{off}}{\lambda_{p0}} - \dfrac{\lambda_w}{n_w \cos\beta_{s0} L_x} \le \dfrac{\lambda_w}{n_w \sin\beta_{s0} L_z} \end{cases} \tag{68}$$

$$\Leftrightarrow \left|\frac{\delta\lambda_{off}}{\lambda_{p0}}\right| \le \frac{\lambda_w}{2n_w \tan\beta_{s0}}\left(\frac{1}{\cos\beta_{s0} L_x} + \frac{1}{\sin\beta_{s0} L_z}\right).$$

The off-Bragg diffraction will occur at $\lambda_{pi} + \delta\lambda_{off}$ only when $\delta\lambda_{off}$ satisfies both Eqs. (65) and (68). However, because $\Delta\lambda_p$ is sufficiently large, every $\delta\lambda_{off}$ within Eq. (68) will always satisfy Eq. (65). Therefore, Eq. (68) could be considered a sufficient condition for $\delta\lambda_{off}$. Similarly, if we choose a proper $\delta\lambda_{off}$ from Eq. (68), every $\delta\beta_{soff}$ within Eq. (62) will always satisfy Eq. (60). Thus, Eq. (62) is considered to be a sufficient condition for $\delta\beta_{soff}$. Consequently, the variable ranges of $\delta\alpha_{soff}$ and $\delta\beta_{soff}$ are determined by Eqs. (61) and (62), respectively. Thus the maximum off-Bragg deviation angles $\delta\alpha_{soffMax(PCR)}$ and $\delta\beta_{soffMax(PCR)}$ are given by

$$\delta\alpha_{soffMax(PCR)} = \frac{\lambda_w}{n_w L_y}, \tag{69}$$

$$\delta\beta_{soffMax(PCR)} = \frac{\lambda_w}{n_w \sin\beta_{s0} L_z}. \tag{70}$$

The above equations imply that the intra-page crosstalk noise in the PCR method does not depend on the hologram dimension L_x. This feature of the PCR method is clearly shown in Fig. 15, where the normalized diffracted intensity is plotted as a function of the position (x_s, y_s) at several values of L_x. While the input image area suffering from the crosstalk noise shrinks with increasing L_x in the conventional monochromatic case, that in the PCR method is unchanged.

3.5.3 Inter-page crosstalk noise

In this section, we will consider the inter-page crosstalk noise which is caused by the unwanted diffraction coming from a grating component in another multiplexed page, i.e., $\mathbf{G}_i + \boldsymbol{\delta}\mathbf{e}_{soff} + \boldsymbol{\delta}\mathbf{e}_{cz} + \boldsymbol{\delta}\mathbf{e}_{cy}$. Similar to the previous section, we obtain the set of inequalities given by

$$-2\tan\beta_{s0}\frac{\delta\lambda_{off}}{\lambda_{p0}} - \frac{\lambda_w}{n_w \cos\beta_{s0} L_x} \le \delta\beta_{soff} \le -2\tan\beta_{s0}\frac{\delta\lambda_{off}}{\lambda_{p0}} + \frac{\lambda_w}{n_w \cos\beta_{s0} L_x}, \tag{71}$$

$$\frac{\delta\alpha_{soff}}{2\sin\beta_{s0}} - \frac{\lambda_w}{2n_w \sin\beta_{s0} L_y} \le \delta\phi_{cz} \le \frac{\delta\alpha_{soff}}{2\sin\beta_{s0}} + \frac{\lambda_w}{2n_w \sin\beta_{s0} L_y}, \tag{72}$$

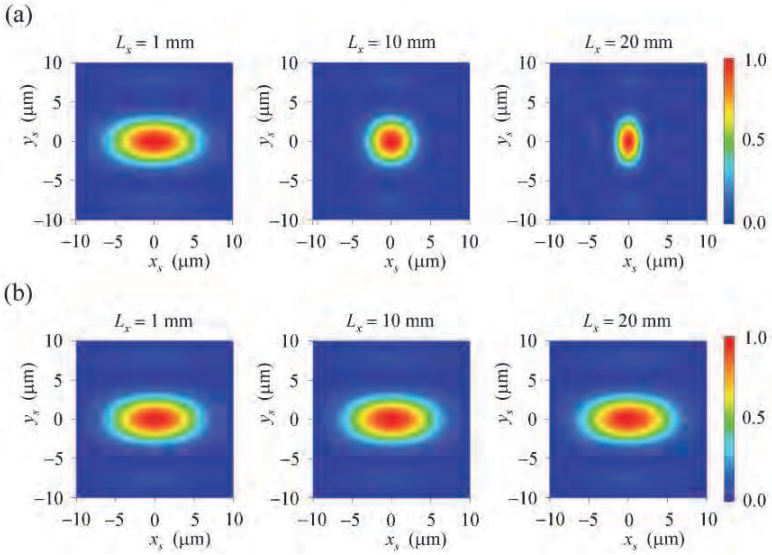

Fig. 15. The input image area suffering from intra-page crosstalk noise in (a) the conventional monochromatic case ($\lambda_w = \lambda_{p0} = 532$ nm, $\Delta\lambda_p = 0$ nm) and (b) the PCR method ($\lambda_w = 532$ nm, $\lambda_{p0} = 815$ nm, $\Delta\lambda_p = 50$ nm). The calculation parameters are as follows: $\beta_{s0} = 30°$; $n_w = 1$; $f_s = 100$ mm; and $L_y = L_z = 10$ mm.

$$-\frac{\delta\beta_{soff}}{2\cos\phi_{cz}} - \frac{\lambda_w}{2n_w\cos\phi_{cz}\sin\beta_{s0}L_z} \le \delta\phi_{cy} \le -\frac{\delta\beta_{soff}}{2\cos\phi_{cz}} + \frac{\lambda_w}{2n_w\cos\phi_{cz}\sin\beta_{s0}L_z}. \tag{73}$$

Note again that the off-Bragg diffraction will occur only when the set of ($\delta\alpha_{soff}$, $\delta\beta_{soff}$, $\delta\phi_{cy}$, $\delta\phi_{cz}$, $\delta\lambda_{off}$) satisfies all of the above inequalities. First, let us consider Eq. (72) to find the rotation angle $\delta\phi_{cz}$ that is large enough to avoid inter-page crosstalk noise. Since the variable range of $\delta\alpha_{soff}$ is expressed as Eq. (63), the off-Bragg diffraction will occur whenever $\delta\phi_{cz}$ satisfies the following inequality:

$$-\frac{\delta\alpha_{sMax} + \delta\alpha_{si}}{2\sin\beta_{s0}} - \frac{\lambda_w}{2n_w\sin\beta_{s0}L_y} \le \delta\phi_{cz} \le \frac{\delta\alpha_{sMax} - \delta\alpha_{si}}{2\sin\beta_{s0}} + \frac{\lambda_w}{2n_w\sin\beta_{s0}L_y}. \tag{74}$$

The above inequality is an expression that is applicable at one particular position (x_{si}, y_{si}) within the input image. In order to avoid crosstalk at every position, the peristrophic rotation angles $\delta\phi_{cz}$ should be set larger than $\delta\phi_{czMin(off)}$; that is,

$$\delta\phi_{czMin(off)} = \frac{\delta\alpha_{sMax}}{\sin\beta_{s0}} + \frac{\lambda_w}{2n_w\sin\beta_{s0}L_y}, \tag{75}$$

where we used the relation $-\delta\alpha_{sMax} \le \delta\alpha_{si} \le \delta\alpha_{sMax}$. The right side in Eq. (75) consists of two parts: one is the minimum peristrophic rotation angle $\delta\phi_{czMin}$ obtained in Section 3.4.1; and the other is the contribution from the off-Bragg diffraction. However, the latter is usually much smaller than the former, and thus the influence of the off-Bragg diffraction can be neglected in

the peristrophic multiplexing. Moreover we should also note that Eq. (75) is applicable in both the monochromatic case and the PCR method. This is consistent with the result in Fig. 11.
Next, we will focus on Eqs. (71) and (73) to find the rotation angle $\delta\phi_{cy}$ that is large enough to avoid crosstalk noise. Before considering the case of PCR, we will again treat the conventional monochromatic readout first. In this case, we can set $\delta\lambda_{off} = 0$. Thus, Eq. (71) is simplified to

$$\left|\delta\beta_{soff}\right| \le \frac{\lambda_w}{n_w \cos\beta_{s0} L_x}. \tag{76}$$

Note that every $\delta\beta_{soff}$ within Eq. (76) always satisfies Eqs. (64). From Eqs. (73) and (76), the off-Bragg diffraction will occur whenever $\delta\phi_{cy}$ satisfies the following inequality:

$$\left|\delta\phi_{cy}\right| \le \frac{\lambda_w}{2n_w \cos\phi_{cz}} \left(\frac{1}{\cos\beta_{s0} L_x} + \frac{1}{\sin\beta_{s0} L_z} \right). \tag{77}$$

Conversely, in order to avoid inter-page crosstalk noise, the crystal rotation angle should be set larger than $\delta\phi_{cyMin(mono)}$; that is,

$$\delta\phi_{cyMin(mono)} = \frac{\lambda_w}{2n_w \cos\phi_{cz}} \left(\frac{1}{\cos\beta_{s0} L_x} + \frac{1}{\sin\beta_{s0} L_z} \right). \tag{78}$$

Now, let us return to the case of the PCR method. Due to the wide spectral width $\Delta\lambda_p$, the restriction of $\delta\beta_{soff}$ in Eq. (71) is considerably relaxed as compared with the monochromatic case; that is,

$$\begin{cases} \tan\beta_{s0} \dfrac{\left(2\delta\lambda_{pi} - \Delta\lambda_p\right)}{\lambda_{p0}} - \dfrac{\lambda_w}{n_w \cos\beta_{s0} L_x} \le \delta\beta_{soff} \\ \delta\beta_{soff} \le \tan\beta_{s0} \dfrac{\left(2\delta\lambda_{pi} + \Delta\lambda_p\right)}{\lambda_{p0}} + \dfrac{\lambda_w}{n_w \cos\beta_{s0} L_x} \end{cases}. \tag{79}$$

On the other hand, the variable range of $\delta\beta_{soff}$ is also limited by the input image size, as is expressed in Eq. (64). Since the off-Bragg diffraction will occur only when $\delta\beta_{soff}$ satisfies both Eqs. (64) and (79), the sufficient condition for $\delta\beta_{soff}$ to produce the off-Bragg diffraction is given by

$$\begin{cases} \max\left[\tan\beta_{s0} \dfrac{\left(2\delta\lambda_{pi} - \Delta\lambda_p\right)}{\lambda_{p0}} - \dfrac{\lambda_w}{n_w \cos\beta_{s0} L_x}, -\delta\beta_{si} - \delta\beta_{sMax} \right] \le \delta\beta_{soff} \\ \delta\beta_{soff} \le \min\left[\tan\beta_{s0} \dfrac{\left(2\delta\lambda_{pi} + \Delta\lambda_p\right)}{\lambda_{p0}} + \dfrac{\lambda_w}{n_w \cos\beta_{s0} L_x}, -\delta\beta_{si} + \delta\beta_{sMax} \right] \end{cases}, \tag{80}$$

where max[*a*, *b*] is a maximum function yielding the larger value between *a* and *b*. If we assume that $\alpha_p = 0$ and take the spectral width required for the full image reconstruction $\Delta\lambda_{BM}$ of Eq. (25) as the probe spectral width $\Delta\lambda_p$, then Eq. (80) can be modified to

$$\begin{cases} -\left(1+\dfrac{\tan\beta_{s0}}{\tan\beta_p}\right)\left(\delta\beta_{si}+\delta\beta_{sMax}\right)-\dfrac{\lambda_w}{n_w\cos\beta_{s0}L_x}\le\delta\beta_{soff} \\ \delta\beta_{soff}\le-\left(1+\dfrac{\tan\beta_{s0}}{\tan\beta_p}\right)\left(\delta\beta_{si}-\delta\beta_{sMax}\right)+\dfrac{\lambda_w}{n_w\cos\beta_{s0}L_x} \end{cases}, \tag{81}$$

where we used the relation of Eq. (20) in the derivation. From Eqs. (73) and (81), the off-Bragg diffraction will occur whenever $\delta\phi_{cy}$ satisfies the following inequality:

$$\begin{cases} \left(1+\dfrac{\tan\beta_{s0}}{\tan\beta_p}\right)\dfrac{\left(\delta\beta_{si}-\delta\beta_{sMax}\right)}{2\cos\phi_{cz}}-\delta\phi_{cyMin(mono)}\le\delta\phi_{cy} \\ \delta\phi_{cy}\le\left(1+\dfrac{\tan\beta_{s0}}{\tan\beta_p}\right)\dfrac{\left(\delta\beta_{si}+\delta\beta_{sMax}\right)}{2\cos\phi_{cz}}+\delta\phi_{cyMin(mono)} \end{cases}. \tag{82}$$

The above inequality is an expression that is applicable at one particular position (x_{si}, y_{si}) within the input image. In order to avoid crosstalk at every position, the crystal rotation angles $\delta\phi_{cy}$ should be set larger than $\delta\phi_{cyMin(PCR)}$; that is,

$$\delta\phi_{cyMin(PCR)}=\left(1+\frac{\tan\beta_{s0}}{\tan\beta_p}\right)\frac{\delta\beta_{sMax}}{\cos\phi_{cz}}+\delta\phi_{cyMin(mono)}, \tag{83}$$

where we used the relation $-\delta\beta_{sMax}\le\delta\beta_{si}\le\delta\beta_{sMax}$. The right side in Eq. (83) consists of the minimum crystal rotation angle $\delta\phi_{cyMin}$ obtained in Section 3.4.2 and the contribution from the off-Bragg diffraction $\delta\phi_{cyMin(mono)}$. Similarly to the peristrophic rotation, the latter is usually much smaller than the former, and thus the influence of the off-Bragg diffraction can be ignored also in the crystal angle multiplexing.

3.6 Storage capacity

Since a single point on the input image corresponds to one particular plane wave in the recording medium, a Fourier hologram stores the information in such a way that one data bit is stored at one localized point in frequency space, and thus, nonlocally in real space. However, due to the off-Bragg diffraction, one data point in frequency space will reproduce an image with a finite dimension in the reconstructed image plane. In order to distinguish two different bits, corresponding data points in frequency space must maintain a certain interval large enough to avoid crosstalk. Therefore, one data bit in real space actually occupies a finite volume in frequency space. If such a volume is denoted by V_{K1bit}, the storage capacity of the holographic memory (N_{bit}) is expressed as

$$N_{bit}=\frac{V_{KG}}{V_{K1bit}}, \tag{84}$$

where V_{KG} is the volume in frequency space which the grating vector can attain through multiplexing. Note that, if the readout wavelength is different from the recording one, as is in the present case, there exists a grating vector that cannot satisfy the Bragg condition with

that probe beam. Such a grating vector should be removed from V_{KG}, because the data stored there cannot be read out. Therefore, the theoretical limit of the storage capacity is ultimately determined by the readout wavelength not the recording one.
Although V_{K1bit} and V_{KG} are generally different in different multiplexing methods, we will consider here the crystal angle multiplexing combined with the peristrophic rotation discussed in Section 3.4. Furthermore, for simplicity, we assume $\alpha_p = 0°$ in this section. First, let us consider V_{KG} after the crystal angle multiplexing around the axis inclined at ϕ_{cz}. The matrix that rotates at ϕ_{cz} around the z-axis, and subsequently rotates at ϕ_{cy} around the y-axis, is expressed as

$$\mathbf{R}\left(\phi_{cy},\phi_{cz}\right)=\begin{pmatrix}\cos\phi_{cy}\cos\phi_{cz} & \cos\phi_{cy}\sin\phi_{cz} & \sin\phi_{cy}\\ -\sin\phi_{cz} & \cos\phi_{cz} & 0\\ -\sin\phi_{cy}\cos\phi_{cz} & -\sin\phi_{cy}\sin\phi_{cz} & \cos\phi_{cy}\end{pmatrix}. \tag{85}$$

The grating vector $k_w(\mathbf{G}_0+\boldsymbol{\delta}\mathbf{e}_{si})$ operated on by that matrix is written as

$$\begin{aligned}\mathbf{R}\left(\phi_{cy},\phi_{cz}\right)k_w\left(\mathbf{G}_0+\boldsymbol{\delta}\mathbf{e}_{si}\right)=2k_w\sin\beta_{s0}&\begin{bmatrix}\cos\phi_{cy}\cos\phi_{cz}\\ -\sin\phi_{cz}\\ -\sin\phi_{cy}\cos\phi_{cz}\end{bmatrix}+k_w\begin{bmatrix}\cos\phi_{cy}\sin\phi_{cz}\\ \cos\phi_{cz}\\ -\sin\phi_{cy}\sin\phi_{cz}\end{bmatrix}\delta\alpha_{si}\\ &+k_w\begin{bmatrix}\cos\beta_{s0}\cos\phi_{cy}\cos\phi_{cz}-\sin\beta_{s0}\sin\phi_{cy}\\ -\cos\beta_{s0}\sin\phi_{cz}\\ -\cos\beta_{s0}\sin\phi_{cy}\cos\phi_{cz}-\sin\beta_{s0}\cos\phi_{cy}\end{bmatrix}\delta\beta_{si}.\end{aligned} \tag{86}$$

If above grating is further rotated around the y-axis by a small angle $\delta\phi_{cy}$, we obtain the differential grating vector ($\boldsymbol{\delta}\mathbf{K}_G$) resulting from small shifts of $\delta\alpha_s$, $\delta\beta_s$, and $\delta\phi_{cy}$:

$$\begin{aligned}&\boldsymbol{\delta}\mathbf{K}_G=k_w\left(\delta\alpha_s\boldsymbol{\delta}\mathbf{e}_{K\alpha s}+\delta\beta_s\boldsymbol{\delta}\mathbf{e}_{K\beta s}+\delta\varphi_{cy}\boldsymbol{\delta}\mathbf{e}_{Kcy}\right),\\ &\boldsymbol{\delta}\mathbf{e}_{K\alpha s}=\begin{bmatrix}\cos\phi_{cy}\sin\phi_{cz}\\ \cos\phi_{cz}\\ -\sin\phi_{cy}\sin\phi_{cz}\end{bmatrix},\ \boldsymbol{\delta}\mathbf{e}_{K\beta s}=\begin{bmatrix}\cos\beta_{s0}\cos\phi_{cy}\cos\phi_{cz}-\sin\beta_{s0}\sin\phi_{cy}\\ -\cos\beta_{s0}\sin\phi_{cz}\\ -\cos\beta_{s0}\sin\phi_{cy}\cos\phi_{cz}-\sin\beta_{s0}\cos\phi_{cy}\end{bmatrix},\\ &\boldsymbol{\delta}\mathbf{e}_{Kcy}=-2\sin\beta_{s0}\begin{bmatrix}\sin\phi_{cy}\cos\phi_{cz}\\ 0\\ \cos\phi_{cy}\cos\phi_{cz}\end{bmatrix}.\end{aligned} \tag{87}$$

Thus, the differential volume in frequency space is given by

$$\begin{aligned}dV_K&=k_w{}^3\left[\left(\boldsymbol{\delta}\mathbf{e}_{K\alpha s}\times\boldsymbol{\delta}\mathbf{e}_{K\beta s}\right)\cdot\boldsymbol{\delta}\mathbf{e}_{Kcy}\right]\delta\alpha_s\delta\beta_s\delta\phi_{cy}\\ &=k_w{}^3\cos\phi_{cz}\sin2\beta_{s0}\delta\alpha_s\delta\beta_s\delta\phi_{cy}.\end{aligned} \tag{88}$$

When we assumed that $\delta\alpha_s$, $\delta\beta_s$, and $\delta\phi_{cy}$ are in the ranges $-\delta\alpha_{sMax} < \delta\alpha_s < \delta\alpha_{sMax}$, $-\delta\beta_{sMax} < \delta\beta_s < \delta\beta_{sMax}$, and $-\delta\phi_{cyMax} < \delta\phi_{cy} < \delta\phi_{cyMax}$, respectively, then V_{KG} after crystal angle multiplexing around the axis inclined at ϕ_{cz}, which is denoted by $V_{KG\_\phi cz}$, can be written as

$$
\begin{aligned}
V_{KG\_\phi cz}(\phi_{cz}) &= \int dV_K \\
&= k_w{}^3 \cos\phi_{cz} \sin 2\beta_{s0} \int_{-\delta\phi_{cyMax}}^{\delta\phi_{cyMax}} d\delta\phi_{cy} \int_{-\delta\alpha_{s\max}}^{\delta\alpha_{s\max}} d\delta\alpha_s \int_{-\delta\beta_{s\max}}^{\delta\beta_{s\max}} d\delta\beta_s \\
&= 8k_w{}^3 \cos\phi_{cz} \sin 2\beta_{s0} \delta\alpha_{s\max} \delta\beta_{s\max} \delta\phi_{cyMax} .
\end{aligned} \tag{89}
$$

Next, let us consider this in combination with peristrophic multiplexing. In this case, crystal angle multiplexing is performed at each inclined angle ϕ_{czn}; that is,

$$
\phi_{czn} = n\delta\phi_{czMin} = n\frac{\delta\alpha_{s\max}}{\sin\beta_{s0}} \quad (n = -n_{\max}, \cdots -2, -1, 0, 1, 2, \cdots n_{\max}), \tag{90}
$$

where $\delta\phi_{czMin}$ is the minimum angular separation in peristrophic multiplexing of Eq. (38); n is an integer; and n_{max} is the maximum integer that satisfies the relation

$$
\phi_{czMax} \geq n_{\max}\frac{\delta\alpha_{s\max}}{\sin\beta_{s0}}, \tag{91}
$$

where ϕ_{czMax} is a maximum peristrophic rotation angle. If we take the summation of $\cos\phi_{czn}$ over all n, we obtain

$$
\begin{aligned}
\sum_{n=-n_{\max}}^{n_{\max}} \cos\phi_{czn} &= \sum_{n=-n_{\max}}^{n_{\max}} \cos\left(n\frac{\delta\alpha_{s\max}}{\sin\beta_{s0}}\right) \\
&= \frac{\cos\left(\dfrac{\delta\alpha_{s\max}}{2\sin\beta_{s0}}\right)}{\sin\left(\dfrac{\delta\alpha_{s\max}}{2\sin\beta_{s0}}\right)} \sin\left[\frac{\delta\alpha_{s\max}}{\sin\beta_{s0}}(n_{\max}+1)\right] - \cos\left[\frac{\delta\alpha_{s\max}}{\sin\beta_{s0}}(n_{\max}+1)\right] \\
&\sim \frac{2\sin\beta_{s0}}{\delta\alpha_{s\max}} \sin\phi_{czMax} - \cos\phi_{czMax} ,
\end{aligned} \tag{92}
$$

where we assumed that $\delta\alpha_{sMax} << 1$ and the relation

$$
\phi_{czMax} \sim \frac{\delta\alpha_{s\max}}{\sin\beta_{s0}}(n_{\max}+1) \tag{93}
$$

approximately holds. Then, V_{KG} after crystal angle multiplexing in combination with peristrophic multiplexing, which is denoted by V_{KG_total}, is expressed as

$$
\begin{aligned}
V_{KG\_total} &= \sum_{n=-n_{\max}}^{n_{\max}} V_{KG\_\phi cz}(\phi_{czn}) \\
&= 8k_w{}^3 \sin 2\beta_{s0} \delta\beta_{s\max} \delta\phi_{cyMax} \left(2\sin\beta_{s0} \sin\phi_{czMax} - \delta\alpha_{s\max} \cos\phi_{czMax}\right)
\end{aligned} \tag{94}
$$

In particular, if we set $\delta\phi_{cyMax} = \phi_{czMax} = \pi/2$, we obtain

$$
V_{KG\_total} = 8\pi k_w{}^3 \sin\beta_{s0} \sin 2\beta_{s0} \delta\beta_{s\max} . \tag{95}
$$

We find that V_{KG_total} increases with increasing maximum deviation angle $\delta\beta_{sMax}$. Note that V_{KG} is, of course, independent of the readout scheme, and thus, Eq. (95) can be applied to both the monochromatic case and the PCR method.

Next, we move on to V_{K1bit}. Let $\delta\alpha_{s1bit}$, $\delta\beta_{s1bit}$, and $\delta\phi_{cy1page}$ denote the angular separations needed to distinguish two different bits or pages. Then V_{K1bit} can be written as

$$V_{K1bit} = k_w{}^3 \cos\phi_{cz} \sin 2\beta_{s0} \delta\alpha_{s1bit} \delta\beta_{s1bit} \delta\phi_{cy1page}. \tag{96}$$

In the monochromatic case, we can adopt $\delta\alpha_{soffMax(mono)}$ in Eq. (66), $\delta\beta_{soffMax(mono)}$ in Eq. (67), and $\delta\phi_{cyMin(mono)}$ in Eq. (78) as $\delta\alpha_{s1bit}$, $\delta\beta_{s1bit}$, and $\delta\phi_{cy1page}$, respectively:

$$\delta\alpha_{s1bit(mono)} = \frac{\lambda_w}{n_w L_y} \tag{97}$$

$$\delta\beta_{s1bit(mono)} = \frac{\lambda_w}{n_w} \min\left[\frac{1}{\cos\beta_{s0} L_x}, \frac{1}{\sin\beta_{s0} L_z}\right] \tag{98}$$

$$\delta\phi_{cy1page(mono)} = \frac{\lambda_w}{2n_w \cos\phi_{cz}} \left(\frac{1}{\cos\beta_{s0} L_x} + \frac{1}{\sin\beta_{s0} L_z}\right) \tag{99}$$

Then, V_{K1bit} for the monochromatic case is given by

$$V_{K1bit(mono)} = \frac{8\pi^3}{L_x L_y L_z} \left(1 + \min\left[\xi, 1/\xi\right]\right), \tag{100}$$

where

$$\xi \equiv \frac{\tan\beta_{s0} L_z}{L_x}. \tag{101}$$

On the other hand, in the case of the PCR method, we similarly adopt $\delta\alpha_{soffMax(PCR)}$ in Eq. (69), $\delta\beta_{soffMax(PCR)}$ in Eq. (70), and $\delta\phi_{cyMin(PCR)}$ in Eq. (83) as $\delta\alpha_{s1bit}$, $\delta\beta_{s1bit}$, and $\delta\phi_{cy1page}$, respectively:

$$\delta\alpha_{s1bit(PCR)} = \frac{\lambda_w}{n_w L_y} \tag{102}$$

$$\delta\beta_{s1bit(PCR)} = \frac{\lambda_w}{n_w \sin\beta_{s0} L_z} \tag{103}$$

$$\begin{aligned} \delta\phi_{cy1page(PCR)} &= \left(1 + \frac{\tan\beta_{s0}}{\tan\beta_p}\right) \frac{\delta\beta_{sMax}}{\cos\phi_{cz}} + \delta\phi_{cy1page(mono)} \\ &\approx \left(1 + \frac{\tan\beta_{s0}}{\tan\beta_p}\right) \frac{\delta\beta_{sMax}}{\cos\phi_{cz}}, \end{aligned} \tag{104}$$

where we assume that the second term at the right side of Eq. (104) is much smaller than the first term and can be neglected. Then V_{K1bit} for the PCR method is given by:

$$V_{K1bit(PCR)} = \frac{16\pi^3 n_w \sin\beta_{s0}}{\lambda_w L_y L_z}\left(\frac{1}{\tan\beta_{s0}} + \frac{1}{\tan\beta_p}\right)\delta\beta_{sMax}\,. \tag{105}$$

Equation (105) does not include L_x but depends on $\delta\beta_{sMax}$ instead. Due to this feature, V_{K1bit} for the PCR method is much larger than that for monochromatic readout. If we rewrite Eq. (105) using $\Delta\lambda_{BM}$ in Eq. (21) and $\delta\lambda_{offMax}$ in Eq. (56), we obtain

$$V_{K1bit(PCR)} = \frac{8\pi^3}{L_x L_y L_z}\frac{\Delta\lambda_{BM}}{\delta\lambda_{offMax}} \tag{106}$$

Therefore, V_{K1bit} for the PCR method is a factor of $\Delta\lambda_{BM} / \delta\lambda_{offMax}$ larger than that in the monochromatic readout. The resultant storage capacity in each readout method is

$$N_{bit(mono)} = \frac{16\pi {n_w}^3 L_x L_y L_z}{{\lambda_w}^3}\frac{\sin^3\beta_{s0}\tan\beta_{s0}}{1+\min\left[\xi, 1/\xi\right]}\delta\beta_{sMax} \tag{107}$$

$$N_{bit(PCR)} = \frac{4\pi {n_w}^2 L_y L_z}{{\lambda_w}^2}\frac{\sin 2\beta_{s0}}{\left(\frac{1}{\tan\beta_{s0}} + \frac{1}{\tan\beta_p}\right)} \tag{108}$$

For example, if λ_w = 532 nm, λ_{p0} = 815 nm, β_{s0} = 30°, n_w = 1, $\delta\beta_{sMax}$ =4.0°, and $L_x = L_y = L_z$ = 10 mm, then β_p = –50°. The resultant storage capacities $N_{bit(mono)}$ and $N_{bit(PCR)}$ are 3.2 Tbit and 4.3 Gbit, respectively. Therefore, the storage capacity in the PCR method decreases by more than two orders of magnitude.

4. Selective detection method

In the previous section, we see that the PCR method causes a significant decrease in the storage capacity. However, such a problem can be overcome if we employ the selective detection method together with PCR (Fujimura et al., 2010). The method is based on the selective detection of a target signal image that is submerged in noise waves. By inserting a suitable wavelength separator into the reconstructed image plane, we can retrieve the stored information without crosstalk even if the angular separation is not large enough to suppress the noise diffraction. In this section, we will explain how to remove the crosstalk noise, and we derive theoretical limit of the storage capacity after the improvement.

4.1 Basic concept and principle

As seen in Fig. 12, the Bragg-matched wavelength at a certain imaging position (x_d, y_d) will change after the crystal rotation of $\delta\phi_{cy}$. From Eq. (43), the amount of shift of the Bragg-matched wavelength $\delta\lambda_{cy\_xfix}$ is expressed as

$$\delta\lambda_{cy\_xfix} = \frac{\lambda_{p0}}{\tan\beta_{s0}}\cos\phi_{cz}\delta\phi_{cy}\,. \tag{109}$$

If we take advantage of this difference of the Bragg-matched wavelength, it should be possible to detect the signal image alone, even if the noise images overlap with the target signal image. For example, let us consider inserting a special wavelength filter into the reconstructed image plane as shown in Fig. 16, whose transmittance T_{LVF} is represented by

$$T_{LVF}(x_d, \lambda) = \mathrm{rect}\left(\frac{\lambda - \lambda_{BMcy}(x_d, y_d, 0, \phi_{cz})}{\Delta\lambda_{LVF}} \right), \tag{110}$$

where λ is the wavelength; $\Delta\lambda_{LVF}$ is the full width of the transmitting band; and rect(x) is the rectangle function defined in Eq. (52). Note that the transmission spectrum of this filter depends on the illuminated location on the filter; that is, the optical waves passing through different spatial positions will undergo different spectral filtering by this filter. Such a wavelength filter is known as a linear variable filter (LVF) since the spectral shift of the transmission band is proportional to the spatial shift of the illuminated position.

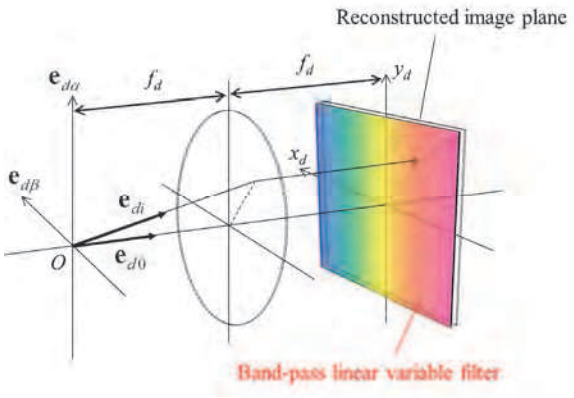

Fig. 16. Configuration for the selective detection method. A special wavelength filter, like a band-pass linear variable filter, is inserted at the reconstructed image plane.

The principle of the selective detection is shown in Fig. 17. Since the transmitting wavelength of the LVF coincides with the spectral dispersion of the target signal image, every diffracted wave that constitutes the signal image can go through the LVF and will be detected by the imager. On the contrary, the LVF will reject the noise diffracted wave whose wavelength lies outside the transmission band of the LVF.

4.2 Theoretical description of the selective detection method

In this section, we will see the influence of the LVF on the properties of the crosstalk noise, and we formulate the achievable storage capacity in the selective detection method. As was seen in Section 3.5.3, the off-Bragg diffraction will occur only when the set of ($\delta\alpha_{soff}$, $\delta\beta_{soff}$, $\delta\phi_{cy}$, $\delta\phi_{cz}$, $\delta\lambda_{off}$) satisfies all of inequalities in Eqs. (71), (72), and (73). Now, due to the transmission band of the LVF, the variable range of $\delta\lambda_{off}$ should be modified to

$$-\frac{\Delta\lambda_{LVF}}{2} \le \delta\lambda_{off} \le \frac{\Delta\lambda_{LVF}}{2}. \tag{111}$$

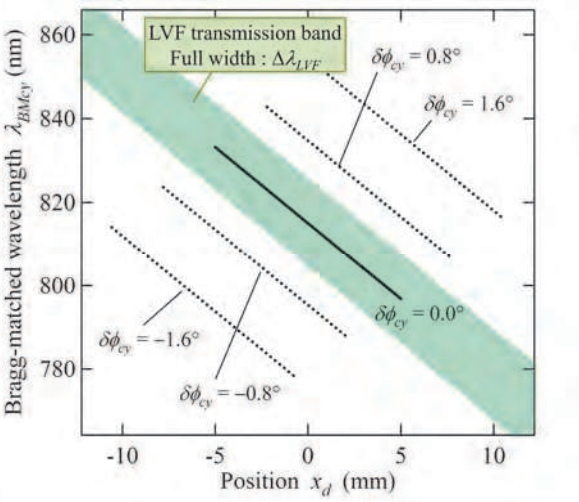

Fig. 17. The concept of the selective detection method. The dotted part of the Bragg-matched line corresponds to the portion of the image that will not be detected by the imager.

Note that the variable range of $\delta\lambda_{off}$ is now independent of the targeting position (x_{si}, y_{si}) within the input image because of the transmitting property of the LVF. In this case, the restriction of $\delta\beta_{soff}$ in Eq. (71) should be changed to

$$\left|\delta\beta_{soff}\right| \le \tan\beta_{s0}\frac{\Delta\lambda_{LVF}}{\lambda_{p0}} + \frac{\lambda_w}{n_w\cos\beta_{s0}L_x}. \tag{112}$$

From Eqs. (73) and (112), we find that the off-Bragg diffraction will occur in the range

$$\left|\delta\phi_{cy}\right| \le \frac{\tan\beta_{s0}}{2\cos\phi_{cz}}\frac{\Delta\lambda_{LVF}}{\lambda_{p0}} + \frac{\lambda_w}{2n_w\cos\phi_{cz}}\left(\frac{1}{\cos\beta_{s0}L_x} + \frac{1}{\sin\beta_{s0}L_z}\right). \tag{113}$$

Therefore, in order to avoid inter-page crosstalk noise, the crystal rotation angle should be set larger than $\delta\phi_{cyMin(SelDet)}$; that is,

$$\begin{aligned}\delta\phi_{cyMin(SelDet)} &= \frac{\tan\beta_{s0}}{2\cos\phi_{cz}}\frac{\Delta\lambda_{LVF}}{\lambda_{p0}} + \frac{\lambda_w}{2n_w\cos\phi_{cz}}\left(\frac{1}{\cos\beta_{s0}L_x} + \frac{1}{\sin\beta_{s0}L_z}\right)\\ &= \frac{\Delta\lambda_{LVF}}{2\Delta\lambda_{BM}}\delta\phi_{cyMin(PCR)} + \delta\phi_{cyMin(mono)},\end{aligned} \tag{114}$$

where $\delta\phi_{cyMin(mono)}$ and $\delta\phi_{cyMin(PCR)}$ are the minimum crystal rotation angle in the monochromatic case and the PCR method, respectively; and we use Eq. (21) to derive the second equality. If we ignore the $\delta\phi_{cyMin(mono)}$, we see that $\delta\phi_{cyMin(SelDet)}$ is improved by a factor of $2\Delta\lambda_{BM}/\Delta\lambda_{LVF}$ than $\delta\phi_{cyMin(PCR)}$. Note that the probe spectral width $\Delta\lambda_p$ need not be equal to the spectral width required for the full image reconstruction $\Delta\lambda_{BM}$ because Eq. (114) no longer includes $\Delta\lambda_p$.

Furthermore, the intra-page crosstalk noise will be also suppressed if $\Delta\lambda_{LVF}$ is sufficiently small. Since the off-Bragg diffraction will occur only when $\delta\beta_{soff}$ satisfies both the inequalities in Eqs. (60) and (62) under the range of Eq. (111), the restriction of $\delta\beta_{soff}$ should be written as

$$\left|\delta\beta_{soff}\right| \le \min\left[\tan\beta_{s0}\frac{\Delta\lambda_{LVF}}{\lambda_{p0}} + \frac{\lambda_w}{n_w\cos\beta_{s0}L_x}, \frac{\lambda_w}{n_w\sin\beta_{s0}L_z}\right]. \tag{115}$$

Therefore, the maximum off-Bragg deviation angles $\delta\alpha_{soffMax(SelDet)}$ and $\delta\beta_{soffMax(SelDet)}$ are obtained as follows:

$$\delta\alpha_{soffMax(SelDet)} = \frac{\lambda_w}{n_w L_y} \tag{116}$$

$$\delta\beta_{soffMax(SelDet)} = \min\left[\tan\beta_{s0}\frac{\Delta\lambda_{LVF}}{\lambda_{p0}} + \frac{\lambda_w}{n_w\cos\beta_{s0}L_x}, \frac{\lambda_w}{n_w\sin\beta_{s0}L_z}\right]. \tag{117}$$

If we adopt $\delta\alpha_{soffMax(SelDet)}$ in Eq.(116), $\delta\beta_{soffMax(SelDet)}$ in Eq. (117), and $\delta\phi_{cyMin(SelDet)}$ in Eq. (114) as $\delta\alpha_{s1bit}$, $\delta\beta_{s1bit}$, and $\delta\phi_{cy1page}$ in Eq. (96), respectively, then V_{K1bit} for the selective detection method is written as

$$V_{K1bit(SelDet)} = \frac{1}{F[\Delta\lambda_{LVF}]}\frac{8\pi^3}{L_xL_yL_z}\left\{1+\min\left[\frac{\xi}{F[\Delta\lambda_{LVF}]},\frac{F[\Delta\lambda_{LVF}]}{\xi}\right]\right\}, \tag{118}$$

where

$$F[\Delta\lambda_{LVF}] \equiv \left(\frac{\Delta\lambda_{LVF}}{2\delta\lambda_{offMax}}+1\right)^{-1} \tag{119}$$

is the improvement factor of the storage capacity. When the condition $\Delta\lambda_{LVF} >> 2\delta\lambda_{offMax}$ holds, Eq. (118) can be simplified to

$$V_{K1bit(SelDet)} = \frac{8\pi^3}{L_xL_yL_z}\frac{\Delta\lambda_{LVF}}{2\delta\lambda_{offMax}}. \tag{120}$$

Comparing this with $V_{K1bit(PCR)}$ in Eq. (106), we find that the storage capacity will be improved by a factor of $2\Delta\lambda_{BM}/\Delta\lambda_{LVF}$. On the other hand, when $\Delta\lambda_{LVF} << 2\delta\lambda_{offMax}$ is satisfied, $V_{K1bit(SelDet)}$ becomes identical to $V_{K1bit(mono)}$. Therefore, the storage capacity in the PCR method will be completely recovered if we use an LVF having a sufficiently small $\Delta\lambda_{LVF}$. However, it should be noted that, in this case, the diffraction efficiency will also decrease with decreasing $\Delta\lambda_{LVF}$. This is because the assumption used to derive Eq. (57) is no longer valid, and the integration range should be modified to $-\Delta\lambda_{LVF}/2 \le \delta\lambda_{off} \le \Delta\lambda_{LVF}/2$:

$$I_{di} \propto \int_{-\frac{\Delta\lambda_{LVF}}{2}}^{\frac{\Delta\lambda_{LVF}}{2}} \mathrm{sinc}^2\left(\frac{\pi\delta\lambda_{off}}{\delta\lambda_{offMax}}\right) I_p\left(\lambda_{pi}+\delta\lambda_{off}\right) d\left(\delta\lambda_{off}\right) \approx \frac{\Delta\lambda_{LVF}}{\Delta\lambda_p} I_{p0}. \tag{121}$$

In order to avoid such reduction in the diffraction efficiency, by considering the spectral width $\delta\lambda_{offMax}$ of the signal diffracted wave, we should set $\Delta\lambda_{LVF} = 2\delta\lambda_{offMax}$. In this case, $V_{K1bit(SelDet)}$ becomes

$$V_{K1bit(SelDet)} = \frac{16\pi^3}{L_xL_yL_z}\left\{1+\min\left[2\xi,\frac{1}{2\xi}\right]\right\}. \tag{122}$$

Since the relation $0 < \min[\xi, 1/\xi] \le 1$ holds, we see that the storage capacity at $\Delta\lambda_{LVF} = 2\delta\lambda_{offMax}$ will reach about half that of the monochromatic case.
From Eqs. (95) and (118), the resultant storage capacity in the selective detection method is

$$N_{bit(selDet)} = \frac{8\pi {n_w}^3 L_xL_yL_z}{{\lambda_w}^3}\frac{F[\Delta\lambda_{LVF}]\sin\beta_{s0}\sin 2\beta_{s0}}{1+\min\left[\frac{\xi}{F[\Delta\lambda_{LVF}]},\frac{F[\Delta\lambda_{LVF}]}{\xi}\right]}\delta\beta_{s\max}. \tag{123}$$

In most cases, $\delta\beta_{sMax}$ is limited by the spectral width $\Delta\lambda_p$ of a given probe light source. Thus, if Eq. (26) is substituted into Eq. (123), we obtain

$$N_{bit(selDet)} = \frac{16\pi {n_w}^3 L_x L_y L_z}{{\lambda_w}^3} \frac{F[\Delta\lambda_{LVF}]}{1+\min\left[\frac{\xi}{F[\Delta\lambda_{LVF}]}, \frac{F[\Delta\lambda_{LVF}]}{\xi}\right]} \frac{\sin^3\beta_{s0}}{\left(1+\frac{\tan\beta_{s0}}{\tan\beta_p}\right)} \frac{\Delta\lambda_p}{\lambda_{p0}}. \quad (124)$$

For example, if $\lambda_w = 532$ nm, $\lambda_{p0} = 815$ nm, $\Delta\lambda_p = 50$ nm, $\beta_{s0} = 30°$, $n_w = 1$, $L_x = L_y = L_z = 10$ mm, and $\Delta\lambda_{LVF} = 2\delta\lambda_{offMax} = 0.043$ nm, then the resultant storage capacity $N_{bit(selDet)}$ is 1.3 Tbit. Therefore, in this case, the storage capacity in the selective detection method reaches 40 percent of the theoretical limit for the monochromatic case.

Finally, the storage capacity in Eq. (124) is plotted as a function of $\Delta\lambda_{LVF}$ in Fig. 18. The improvement starts at $\Delta\lambda_{LVF} = 100$ nm, then the storage capacity increases linearly with increasing $\Delta\lambda_{LVF}$, and finally, it asymptotically approaches the theoretical limit of the monochromatic case. Note that the kink observed at $\Delta\lambda_{LVF} = 0.06$ nm is derived from the minimum function; that is to say, from that point on, the storage capacity further increases due to the reduction of the intra-page crosstalk noise $\delta\beta_{soffMax}$ in Eq. (117).

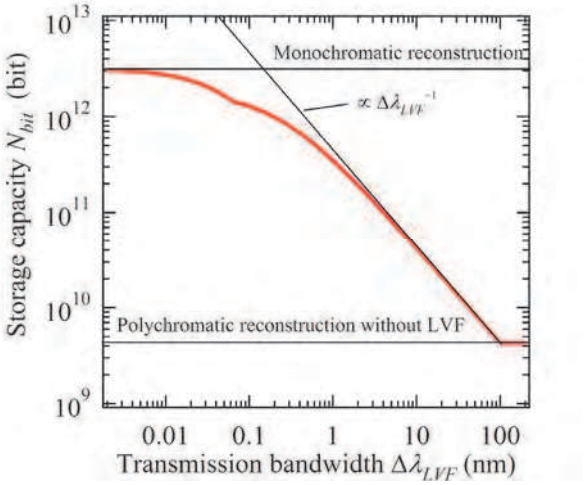

Fig. 18. Storage capacity as a function of transmission bandwidth $\Delta\lambda_{LVF}$. The calculation parameters are as follows: $\lambda_w = 532$ nm, $\lambda_{p0} = 815$ nm, $\Delta\lambda_p = 50$ nm, $\beta_{s0} = 30°$, $n_w = 1$, and $L_x = L_y = L_z = 10$ mm.

5. Summary

We have developed the theory of holographic reconstruction with polychromatic light. In particular, focusing on its application to holographic memory, the required spectral width, distortion of the reconstructed image, diffraction efficiency, intra- and inter-page crosstalk, and storage capacity were investigated. The obtained results are summarized below.

The required spectral width and image distortion

A larger input image (x_{sMax}, y_{sMax}) or smaller focal length f_s require a larger spectral width $\Delta\lambda_{BM}$ to reconstruct the whole image. Generally the required spectral width depends on both directions x_{sMax} and y_{sMax}, but if the signal, reference, and probe beams lie in the same plane ($\alpha_p = 0°$), it becomes independent of y_{sMax}. Furthermore, the condition $\alpha_p = 0°$ minimizes the image distortion, where the image is magnified by the wavelength ratio μ_0 in the y_d-direction, but is unchanged in the x_d-direction.

Multiplexing method

Crystal angle multiplexing used in combination with peristrophic multiplexing is the most suitable multiplexing method in polychromatic reconstruction (PCR). Other multiplexing methods are also possible in principle, but most of them require a complicated system to read a target page because the diffracted wave $\mathbf{e}_{d0}$ will be pointed in a different direction at each multiplexed page.

Diffraction efficiency

Since the grating component can diffract only a limited spectral component, the diffraction efficiency, which is defined here as the ratio of the diffracted power by one grating component to the total power of the input probe beam, is much smaller than in the conventional monochromatic readout. This may be an unavoidable drawback of the PCR method.

Intra- and Inter-page crosstalk noise

Due to the wide spectral width of the probe beam, the hologram dimension L_x does not influence the intra-page crosstalk noise, and thus the input image area suffering from the intra-page crosstalk noise is slightly enlarged. On the other hand, the inter-page crosstalk noise is a crucial problem in the PCR method. The angular Bragg selectivity is greatly degraded, and thus, the storage capacity decreases by more than two orders of magnitude. However, this problem can be solved by using the selective detection method mentioned below.

Selective detection method and the achievable storage capacity

Taking advantage of the wavelength difference after the crystal rotation, we can detect the signal image alone, even if the noise images overlap with the target signal image. The storage capacity when employing the selective detection method reached 40 percent of the theoretical limit for the monochromatic case.

PCR is a unique and useful method for holographic memory systems. While other nondestructive readout methods have failed to achieve a high storage capacity, we theoretically proved that PCR, when used in combination with the selective detection method, enables us to achieve both nondestructive readout and a high storage capacity, simultaneously.

6. References

Barbastathis, G. & Psaltis, D., (2000). Volume holographic multiplexing methods, In: *Holographic data storage*, Coufal, H.J., Psaltis, D., & Sincerbox, G.T., pp. 21-62, Springer, 978-3540666912, New York.

Champagne, E.B. (1967). Nonparaxial imaging magnification and aberration properties in holography. *Journal of the Optical Society of America*, Vol. 57, No. 1, pp.51-55

Curtis, K., Pu, A., & Psaltis, D. (1994). Method for holographic storage using peristrophic multiplexing. *Optics Letters*, Vol. 19, No. 13, pp.993-994

Fujimura, R., Shimura, T., & Kuroda, K. (2007). Polychromatic reconstruction for volume holographic memory. *Optics Letters*, Vol. 32, No. 13, pp.1860-1862

Fujimura, R., Shimura, T., & Kuroda, K. (2010). Multiplexing capability in polychromatic reconstruction with selective detection method. *Optics Express*, Vol. 18, No. 2, pp.1091-1098

Gulanyan, E.K., Dorosh, I.R., Iskin, V.D., Mikaelyan, A.L., & Maiorchuk, M.A. (1979). Nondestructive readout of holograms in iron-doped lithium niobate crystals. *Soviet Journal of Quantum Electronics*, Vol. 9, No. 5, pp.647-649

Külich, H.C. (1987). A new approach to read volume holograms at different wavelengths. *Optics Communications*, Vol. 64, No. 5, pp.407-411

Petrov, M.P., Stepanov, S.I., & Kamshilin, A.A. (1979). Holographic storage of information and peculiarities of light diffraction in birefringent electro-optic crystals. *Optics and Laser Technology*, Vol. 11, No. 3, pp.149-151

van Heerden, P.J. (1963). Theory of optical information storage in solids. *Applied Optics*, Vol. 2, No. 4, pp.393-400

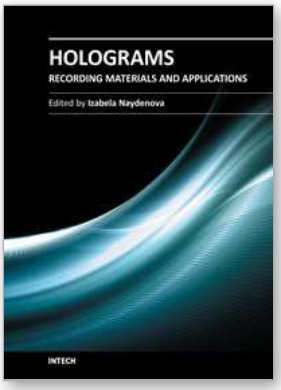

Holograms - Recording Materials and Applications

Edited by Dr Izabela Naydenova

ISBN 978-953-307-981-3
Hard cover, 382 pages
Publisher InTech
Published online 09, November, 2011
Published in print edition November, 2011

Holograms - Recording Materials and Applications covers recent advances in the development of a broad range of holographic recording materials including ionic liquids in photopolymerisable materials, azo-dye containing materials, porous glass and polymer composites, amorphous chalcogenide films, Norland optical adhesive as holographic recording material and organic photochromic materials. In depth analysis of collinear holographic data storage and polychromatic reconstruction for volume holographic memory are included. Novel holographic devices, as well as application of holograms in security and signal processing are covered. Each chapter provides a comprehensive introduction to a specific topic, with a survey of developments to date.

InTech Europe
University Campus STeP Ri
Slavka Krautzeka 83/A
51000 Rijeka, Croatia
Phone: +385 (51) 770 447
Fax: +385 (51) 686 166
www.intechopen.com

InTech China
Unit 405, Office Block, Hotel Equatorial Shanghai
No.65, Yan An Road (West), Shanghai, 200040, China
中国上海市延安西路65号上海国际贵都大饭店办公楼405单元
Phone: +86-21-62489820
Fax: +86-21-62489821